

# Structured Tensor Decomposition Based Channel Estimation and Double Refinements for Active RIS Empowered Broadband Systems

Yirun Wang, Yongqing Wang, Yuyao Shen, Gongpu Wang, and Chintha Tellambura, *Fellow, IEEE*

arXiv:2411.16420v1 [cs.IT] 25 Nov 2024

**Abstract**—Channel parameter estimation is crucial for optimal designs of next-generation reconfigurable intelligent surface (RIS)-empowered communications and sensing. Tensor-based mechanisms are particularly effective, capturing the multi-dimensional nature of wireless channels, especially in scenarios where RIS integrates with multiple-antenna devices. However, existing studies assume either a line-of-sight (LOS) scenario or a blocked condition for non-RIS channel. This paper solves a novel problem: tensor-based channel parameter recovery for active RIS-aided multiple-antenna wideband connections in a multipath environment with non-RIS paths. System settings are customized to construct the received signals as a fifth-order canonical polyadic (CP) tensor. Four of the five-factor matrices unfortunately contain redundant columns, and the remaining one is a Vandermonde matrix, which fails to satisfy the Kruskal condition for tensor decomposition uniqueness. To address this issue, spatial smoothing and Vandermonde structured CP decomposition (VSCPD) are applied, making the tensor factorization problem solvable and providing a relaxed general uniqueness condition. A sequential triple-stage channel estimation framework is proposed based on the factor estimates. The first stage enables multipath identification and algebraic coarse estimation, while the following two stages offer optional successive refinements at the cost of increased complexity. The closed-form Cramér-Rao lower bound (CRLB) is derived to assess the estimation performance. Herein, the noise covariance matrix depends on multipath parameters in our active-RIS scenario. Finally, numerical results are provided to verify the effectiveness of proposed algorithms under various evaluation metrics.

**Index Terms**—Channel estimation, multipath parameter, reconfigurable intelligent surface, sequential refinement, tensor decomposition, Vandermonde matrix.

## I. INTRODUCTION

Reconfigurable intelligent surface (RIS) is a key technology for 5G/6G and beyond, capable of intelligently customizing the radio propagation environment and enhancing signal transmission coverage [1], [2]. Typically, RIS is a planar array composed of multiple reflection elements, each programmable to adjust the amplitude and phase shift of incident signals [3]. Optimally designing the RIS reflection coefficients allows

desired signals to be efficiently amplified [4], making RIS a promising solution to mitigate severe path loss in millimeter wave (mmWave) communications. Additionally, RIS can serve as a high-resolution reference point [5], reducing reliance on conventional anchors in positioning systems.

Across the literature, RIS is categorized into several types, e.g., (nearly)-passive RIS [6], active RIS [7], hybrid RIS [8] (composed of reflectors and sensors), among others.

As a two-dimensional (2D) metasurface, the channel between an RIS and a single-antenna radio can naturally be modeled as a matrix. Complementing RIS, additional spatial dimensions are provided by the high-profile multiple-antenna technology that enables to enhance channel capacity and achieve diversity gain [9]. Furthermore, orthogonal frequency-division multiplexing (OFDM) offers an extra channel dimension – the frequency domain, yielding superior robustness against multipath fading and improved spectrum efficiency [10]. Therefore, when RIS is integrated with multiple-antenna OFDM systems, the transmission channel can be effectively represented as a multi-dimensional array, i.e., tensor.

Accurate channel state information (CSI) is essential for the optimal design of RIS-empowered wireless networks. Recently, tensor-based channel estimation (CE) techniques have been extensively explored. These methods excel because they naturally capture multi-dimensional channels [11], decouple unknowns in each dimension [12], and deliver precise estimation performance [13]. Generally, CE can be implemented in two ways. The first approach directly recovers the coefficients in channel tensors or matrices [14]–[16]. The second approach models the channels using path-specific parameters such as path gain, delay, and angles of arrival and departure (AOA/AOD) [17]. This strategy transforms the original CE problem into a parameter recovery issue. In particular, due to the sparse scattering nature in the mmWave scenarios, the number of transmission paths is limited [18], resulting in fewer unknown multipath parameters than channel coefficients. Additionally, acquiring channel parameters is crucial for subsequent tasks like target localization and environment mapping [19]. Therefore, this paper focuses on the second approach, emphasizing parameter retrieval.

There are several related works on tensor-based channel parameter estimation for RIS systems. Study [20] developed an algebraic solution without iterations for hybrid-RIS systems. However, a hybrid RIS setup requires an extra controller for inter-equipment cooperation, increasing the complexity of the implementation. The work in [21] proposed to turn off partial

Yirun Wang, Yongqing Wang, and Yuyao Shen are with the School of Information and Electronics, Beijing Institute of Technology, Beijing 100081, China (e-mail: yrwang719@163.com; wangyongqing@bit.edu.cn; syxyz@gmail.com).

Gongpu Wang is with the Beijing Key Laboratory of Transportation Data Analysis and Mining, Beijing Jiaotong University, Beijing 100044, China (e-mail: gpwang@bjtu.edu.cn).

Chintha Tellambura is with the Department of Electrical and Computer Engineering, University of Alberta, Edmonton, AB T6G 2R3, Canada (e-mail: ct4@ualberta.ca).

Corresponding author: Yuyao Shen.

RIS elements to save pilot overhead and capitalized on extrapolation to complete the channel estimate. The work in [22] studied the direct recovery of channel parameters from signal tensor without the intermediate tensor factorization process. In addition, studies [23]–[25] investigated the Vandermonde structured canonical polyadic decomposition (VSCPD)-based CE mechanisms. The VSCPD leverages the nature of Vandermonde factor matrices, offering accurate decomposition result with cheaper complexity compared to conventional alternating least squares (ALS)-CPD algorithm [26]. The work in [23] put forth a twin-RIS structure and constructed a signal tensor with rank proportional to RIS element number, thus requiring significant training overhead. Study [24] addressed this issue and significantly reduced the tensor rank to multipath number. Reference [25] further considered a mobile user and investigated the Doppler estimation problem. However, [24], [25] resorted to computationally expensive 2D search to acquire parameters, as they only constructed a third-order tensor and failed to form a higher-order one.

Importantly, all the related works above assumed that the direct channel between user equipment (UE) and base station (BS) was blocked due to unfavorable environmental conditions, and the UE-BS connection entirely depended on the RIS to create an additional cascaded UE-RIS-BS link. As such, these conventional algorithms were tailored for the CE of the cascaded UE-RIS-BS channel, benefiting from the problem simplification introduced by such block assumption. Under such a framework, when the direct UE-BS channel exists in other scenarios, its estimation requires to turn off all RIS elements [27], [28], increasing the implementational step and complexity. To this end, the work in [29] considered the existence of a direct UE-BS link and utilized sequential CPDs to recover parameters of both direct and cascade channels. Herein, the active RIS was deployed, enabling signal reflection and amplification. Active RIS can adjust the strength of the cascaded channel to avoid its overwhelming dominance on the direct channel and thus can remarkably improve the system performance over the passive RIS [30], [31]. However, study [29] only focused on the line-of-sight (LOS) scenario, and its CE algorithm undoubtedly degrades in the multipath case.

Motivated by the above, we extend the system model in [29] to the general multipath scenario and investigate the channel parameter acquisition issue. We formulate a CE scenario with active RIS deployed onto an unmanned aerial vehicle (UAV) to assist the uplink communications in a single-input multiple-output (SIMO)-OFDM system (Fig. 1). We consider the fully-multipath case, i.e., frequency-selective channels for UE-BS, UE-RIS, and RIS-BS links. Owing to the UAV-mounted RIS's agile state, the RIS-BS channel's CSI stays unavailable. Both RIS and BS are assumed to form uniform planar array (UPA) topologies. The contributions of this work are summarized as follows.

- We carefully design the transmission pilots, RIS profile, and combining matrix. Consequently, the stacked received signals can be expressed as a Kronecker product of five vectors, which can be further transformed into a fifth-order canonical polyadic (CP) tensor.
- Among the CP factors, the first is a Vandermonde matrix,

while the other four possess repeated columns. This configuration renders the direct CPD inapplicable under the classical Kruskal's uniqueness condition. To address this issue, spatial smoothing, and VSCPD are employed to enable tensor factorization, achieving both fast speed and desirable accuracy. A relaxed general uniqueness condition is provided, resulting in a loose demand relevant only to spatial-smoothing parameters for our case.

- A tri-stage CE framework is proposed using the estimates of factor matrices. The first stage performs multipath identification and gives an algebraic coarse solution. Each of the subsequent two stages is optional, refining the estimation accuracy sequentially via search or iteration, thus at the expense of complexity growth.
- We derive the closed-form Cramér-Rao lower bound (CRLB). Owing to the additional introduction of thermal noise at active RIS, the covariance matrix of total received noise is also a function of multipath parameters. The CRLB analysis in the conventional passive-RIS scenario is a particular case of ours with the active RIS.

The remainder of this paper is organized as follows. Section II presents the channel and signal models. Section III describes tensor construction, VSCPD with spatial smoothing, and our triple-stage CE framework. Section IV derives CRLB and analyzes algorithm complexity. Section V provides numerical results and Section VI concludes this paper. The main acronyms are listed in Acronyms at the end of this paper.

*Notations:* Scalars, vectors, matrices, tensors, and sets are denoted by  $a$ ,  $\mathbf{a}$ ,  $\mathbf{A}$ ,  $\mathcal{A}$ , and  $\mathcal{A}$ , respectively.  $\mathbb{R}$  and  $\mathbb{C}$  denote the real and complex domains, respectively. The transpose, complex conjugate, conjugate transpose, inverse, and pseudo-inverse are denoted by  $(\cdot)^T$ ,  $(\cdot)^*$ ,  $(\cdot)^H$ ,  $(\cdot)^{-1}$ , and  $(\cdot)^\dagger$ , respectively. Vectorization, reverse vectorization, and trace are denoted by  $\text{vec}(\cdot)$ ,  $\text{unvec}(\cdot)$ ,  $\text{tr}(\cdot)$ , respectively. Real part, imaginary part, and amplitude are denoted by  $\Re(\cdot)$ ,  $\Im(\cdot)$ , and  $|\cdot|$  respectively, and  $j^2 = -1$ .  $\text{diag}\{\mathbf{a}\}$  denotes the diagonal matrix formed by  $\mathbf{a}$ .  $\underline{\mathbf{A}}$  is the submatrix deleting the last row of  $\mathbf{A}$ .  $\|\cdot\|$ ,  $\|\cdot\|_F$ ,  $[\cdot]$ , and  $\mathbb{E}[\cdot]$  denote the Euclidean norm, Frobenius norm, CPD operator, and statistical expectation, respectively. Symbols  $\circ$ ,  $\otimes$ ,  $\odot$ , and  $\otimes$  denote the outer product, Kronecker product, Khatri–Rao product, and Hadamard product, respectively.  $\mathbf{1}$ ,  $\mathbf{0}$ , and  $\mathbf{I}$  denote the all-one, all-zero, and identity matrices, respectively.  $\text{rank}(\mathbf{A})$  and  $k_{\mathbf{A}}$  denote the matrix rank and Kruskal rank (or  $k$ -rank) of  $\mathbf{A}$ , respectively. Finally,  $\mathcal{N}(\boldsymbol{\mu}, \boldsymbol{\Sigma})$  and  $\mathcal{CN}(\boldsymbol{\mu}, \boldsymbol{\Sigma})$  denote real and complex Gaussian distributions with mean  $\boldsymbol{\mu}$  and variance  $\boldsymbol{\Sigma}$ , respectively.

*Vandermonde matrix:* Matrix  $\mathbf{A} \in \mathbb{C}^{I \times R}$  is called a Vandermonde matrix if  $[\mathbf{A}]_{i,r} = e^{j(i-1)\omega_r}$ , and  $\{\omega_r\}_{r=1}^R$  are its generators.

## II. PROBLEM FORMULATION

This work considers attaching an RIS to a UAV to assist uplink communications from a UE to the BS – Fig. 1. The fully-multipath scenario is assumed, including the presence of a direct UE-BS channel, to address the general CE issue. Additionally, the UE is assumed to be a single-antenna radio.

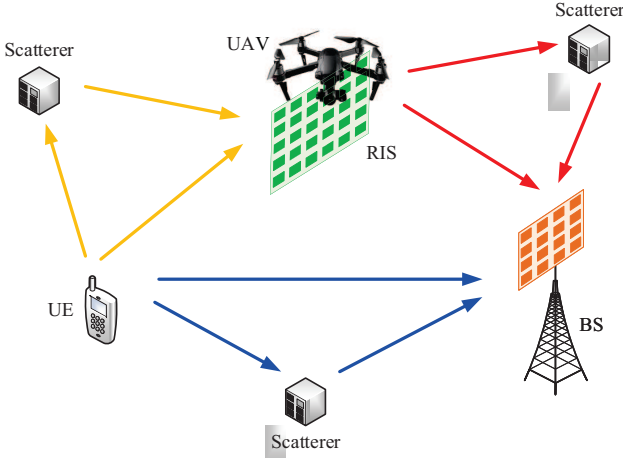


Fig. 1. Illustration of a UAV-mounted RIS-assisted uplink wireless system with multipath channels.

Meanwhile, both BS and RIS employ UPA of sizes  $\tilde{N}_y \times \tilde{N}_z$  and  $M_y \times M_z$ , respectively, located on the YOZ plane in their local coordinate systems (LCSs). The differences between our UAV-mounted RIS case and fixed RIS one are presented at the end of this section.

This paper resorts to the active RIS, whose each element comprises a phase shifter and an active amplifier for incident signals. The amplification coefficients of RIS elements are assumed to remain identical and denoted by unified notation  $\eta > 1$ . It is worth noting that the signal amplification at the active RIS introduces thermal noise at the same time. The energy consumption of active RIS can be modeled as [32]

$$P_R = (\eta^2 - 1)M_y M_z (P_{in} + \sigma_R^2), \quad (1)$$

where  $P_{in}$  is the average power of incident signals at each RIS element, and  $\sigma_R^2$  denotes the power of the thermal noises generated from every RIS element.

#### A. Channel Model

This paper considers an OFDM wideband wireless system over frequency-selective fading channels. The channel frequency responses (CFRs) for the UE-BS, UE-RIS, and RIS-BS links associated with the  $k$ th subcarrier are denoted by  $\mathbf{h}_L^{(k)} \in \mathbb{C}^{\tilde{N}_y \tilde{N}_z \times 1}$ ,  $\mathbf{h}_{R,1}^{(k)} \in \mathbb{C}^{M_y M_z \times 1}$ , and  $\mathbf{H}_{R,2}^{(k)} \in \mathbb{C}^{\tilde{N}_y \tilde{N}_z \times M_y M_z}$  respectively,  $k = 1, \dots, K_0$  with total  $K_0$  subcarriers. The channels are formulated using geometry-related multipath parameters as

$$\mathbf{h}_L^{(k)} = \sum_{\ell=1}^L \beta_L^{(\ell)} e^{-j2\pi f^{(k)} \tau_L^{(\ell)}} \mathbf{a}_B(\boldsymbol{\theta}_L^{(\ell)}), \quad (2)$$

$$\mathbf{h}_{R,1}^{(k)} = \sum_{p=1}^P \beta_{R,1}^{(p)} e^{-j2\pi f^{(k)} \tau_{R,1}^{(p)}} \mathbf{a}_R(\boldsymbol{\varphi}_A^{(p)}), \quad (3)$$

$$\mathbf{H}_{R,2}^{(k)} = \sum_{q=1}^Q \beta_{R,2}^{(q)} e^{-j2\pi f^{(k)} \tau_{R,2}^{(q)}} \mathbf{a}_B(\boldsymbol{\theta}_R^{(q)}) \mathbf{a}_R^T(\boldsymbol{\varphi}_D^{(q)}), \quad (4)$$

where  $L$ ,  $P$ , and  $Q$  denote the number of paths for UE-BS, UE-RIS, and RIS-BS channels, respectively,  $\beta_L^{(\ell)}$ ,  $\beta_{R,1}^{(p)}$ ,

and  $\beta_{R,2}^{(q)}$  represent the path gains,  $\tau_L^{(\ell)}$ ,  $\tau_{R,1}^{(p)}$ , and  $\tau_{R,2}^{(q)}$  denote channel delays,  $f^{(k)} = (k-1)\Delta_f$  is subcarrier frequency with  $\Delta_f$  being frequency spacing,  $\mathbf{a}_B \in \mathbb{C}^{\tilde{N}_y \tilde{N}_z \times 1}$  and  $\mathbf{a}_R \in \mathbb{C}^{M_y M_z \times 1}$  are the array responses of BS and RIS, respectively,  $\boldsymbol{\theta}_L^{(\ell)} = [\theta_{L,az}^{(\ell)}, \theta_{L,el}^{(\ell)}]^T$  and  $\boldsymbol{\theta}_R^{(\ell)} = [\theta_{R,az}^{(\ell)}, \theta_{R,el}^{(\ell)}]^T$  denote the AOA pairs of BS for UE-BS and RIS-BS channels, respectively, with each pair containing an azimuth angle and an elevation angle, similarly  $\boldsymbol{\varphi}_A^{(p)} = [\varphi_{A,az}^{(p)}, \varphi_{A,el}^{(p)}]^T$  and  $\boldsymbol{\varphi}_D^{(q)} = [\varphi_{D,az}^{(q)}, \varphi_{D,el}^{(q)}]^T$  represent RIS's AOA and AOD pairs for the UE-RIS and RIS-BS channels.

The spatial array response is formulated as follows. Take the RIS's one as a detailed example. Without loss of generality, assume the RIS elements start from the local coordinate origin. Out of unified expression, temporarily remove some subscripts and superscripts for specific individuals, and  $\mathbf{a}_R(\boldsymbol{\varphi})$  can be formed from

$$[\mathbf{a}_R(\boldsymbol{\varphi})]_m = e^{j\frac{2\pi}{\lambda} [\mathbf{P}_R]_{m,:} \mathbf{d}(\boldsymbol{\varphi})}, \quad m = 1, \dots, M_y M_z, \quad (5)$$

where  $\mathbf{P}_R = [\mathbf{0}_{M_y M_z \times 1}, \mathbf{y}_R \otimes \mathbf{1}_{M_z \times 1}, \mathbf{1}_{M_y \times 1} \otimes \mathbf{z}_R] \in \mathbb{R}^{M_y M_z \times 3}$  vertically stacks the local three-dimensional (3D) positions of every RIS element,  $\mathbf{y}_R \in \mathbb{R}^{M_y \times 1}$  and  $\mathbf{z}_R \in \mathbb{R}^{M_z \times 1}$  denote the local Y positions and Z positions of RIS elements, respectively,  $\lambda$  is the signal wavelength, and  $\mathbf{d}(\boldsymbol{\varphi}) = [\cos(\varphi_{az}) \cos(\varphi_{el}), \sin(\varphi_{az}) \cos(\varphi_{el}), \sin(\varphi_{el})]^T$  represents the direction vector of the arrival/departure signal. Further, assume the RIS array is uniformly spaced on both two axes with identical element spacing  $d_R$ , then (5) can be recast as

$$\mathbf{a}_R(\boldsymbol{\varphi}) = \mathbf{a}^{(M_y)}(\omega_2) \otimes \mathbf{a}^{(M_z)}(\omega_3), \quad (6)$$

where  $[\mathbf{a}^{(M)}(\omega)]_m = e^{j(m-1)\omega}$ ,  $m = 1, \dots, M$ , and

$$\omega_2 = \frac{2\pi}{\lambda} d_R \sin(\varphi_{az}) \cos(\varphi_{el}), \quad \omega_3 = \frac{2\pi}{\lambda} d_R \sin(\varphi_{el}). \quad (7)$$

Analogously, the array response  $\mathbf{a}_B(\boldsymbol{\theta})$  of BS can be expressed as

$$\mathbf{a}_B(\boldsymbol{\theta}) = \mathbf{a}^{(\tilde{N}_y)}(\omega_4) \otimes \mathbf{a}^{(\tilde{N}_z)}(\omega_5), \quad (8)$$

$$\omega_4 = \frac{2\pi}{\lambda} d_B \sin(\theta_{az}) \cos(\theta_{el}), \quad \omega_5 = \frac{2\pi}{\lambda} d_B \sin(\theta_{el}), \quad (9)$$

and we denote the BS's position matrix and element spacing by  $\mathbf{P}_B$  and  $d_B$ , respectively.

#### B. Signal Model

Consider that the UE transmits  $G$  OFDM symbols to the BS in the time domain. We assume that the active-RIS profile  $\boldsymbol{\gamma}^{(g)} = \eta [e^{j\theta_1^{(g)}}, \dots, e^{j\theta_{M_y M_z}^{(g)}}]^T \in \mathbb{C}^{M_y M_z \times 1}$  changes at every distinct time slot  $g$ ,  $g = 1, \dots, G$  by adjusting phase shifts, and let  $\boldsymbol{\Gamma}^{(g)} = \text{diag}(\boldsymbol{\gamma}^{(g)})$ . The received baseband signal for the  $k$ th subcarrier the  $g$ th slot is given by

$$\tilde{\mathbf{y}}^{(k,g)} = \mathbf{R}^H (\mathbf{h}_L^{(k)} + \mathbf{h}_{R,1}^{(k,g)}) x^{(k,g)} + \mathbf{w}^{(k,g)}, \quad (10)$$

where  $\mathbf{R} \in \mathbb{C}^{\tilde{N}_y \tilde{N}_z \times N_1 N_2}$  denotes the combining matrix,  $x^{(k,g)}$  is the transmitted signal with transmit power  $|x^{(k,g)}|^2 = P_T$ ,  $\mathbf{h}_{R,1}^{(k,g)} = \mathbf{H}_{R,2}^{(k)} \boldsymbol{\Gamma}^{(g)} \mathbf{h}_{R,1}^{(k)}$  denotes the cascaded UE-RIS-BS channel, and the overall received noise  $\mathbf{w}$  is expressed as

$$\mathbf{w}^{(k,g)} = \mathbf{R}^H (\mathbf{w}_B^{(k,g)} + \mathbf{H}_{R,2}^{(k)} \boldsymbol{\Gamma}^{(g)} \mathbf{w}_R^{(k,g)}), \quad (11)$$

where  $\mathbf{w}_B^{(k,g)} \sim \mathcal{CN}(\mathbf{0}_{\tilde{N}_y \tilde{N}_z \times 1}, \sigma_B^2 \mathbf{I}_{\tilde{N}_y \tilde{N}_z})$  denotes the received thermal noise at BS with noise power  $\sigma_B^2$ , and  $\mathbf{w}_R^{(k,g)} \sim \mathcal{CN}(\mathbf{0}_{M_y M_z \times 1}, \sigma_R^2 \mathbf{I}_{M_y M_z})$  is the thermal noise incurred by active RIS elements. Noises  $\mathbf{w}_B^{(k,g)}$  and  $\mathbf{w}_R^{(k,g)}$  are uncorrelated to each other. Notably,  $\mathbf{w}^{(k,g)}$  depends on the unknown RIS-BS channel  $\mathbf{H}_{R,2}^{(k)}$  here in our active-RIS scenario, and (11) degrades into the conventional passive-RIS case if removing the second noise term. These noise results are important for the bounding issue in Section IV-A.

Introducing (3)–(4), cascaded channel  $\mathbf{h}_R^{(k,g)}$  in (10) further becomes

$$\mathbf{h}_R^{(k,g)} = \sum_{p=1}^P \sum_{q=1}^Q \beta_R^{(p,q)} \rho_R^{(p,q)} e^{-j2\pi f^{(k)} \tau_R^{(p,q)}} \mathbf{a}_B(\boldsymbol{\theta}_R^{(q)}), \quad (12)$$

where  $\beta_R^{(p,q)} = \beta_{R,1}^{(p)} \beta_{R,2}^{(q)}$  denotes the cascaded path gain,  $\tau_R^{(p,q)} = \tau_{R,1}^{(p)} + \tau_{R,2}^{(q)}$  represents the cascaded delay, and

$$\rho_R^{(p,q)} = (\boldsymbol{\gamma}^{(g)})^T (\mathbf{a}_R(\varphi_A^{(p)}) \otimes (\mathbf{a}_R(\varphi_D^{(q)}))). \quad (13)$$

Recall (6) and therein we restore individual subscripts and superscripts, then (13) can be rewritten as [33, Eq. (4)]

$$\rho_R^{(p,q)} = (\boldsymbol{\gamma}^{(g)})^T (\mathbf{a}^{(M_y)}(\omega_2^{(p,q)}) \otimes \mathbf{a}^{(M_z)}(\omega_3^{(p,q)})), \quad (14)$$

where  $\omega_2^{(p,q)} = \omega_{A,2}^{(p)} + \omega_{D,2}^{(q)} = \frac{2\pi}{\lambda} d_R \psi_2^{(p,q)}$  and  $\omega_3^{(p,q)} = \omega_{A,3}^{(p)} + \omega_{D,3}^{(q)} = \frac{2\pi}{\lambda} d_R \psi_3^{(p,q)}$  denote the effective RIS-incurred phase-shift spacings along the Y and Z axes, respectively, with intermediate angle-related parameters defined as

$$\begin{aligned} \psi_2^{(p,q)} &= \sin(\varphi_{A,az}^{(p)}) \cos(\varphi_{A,el}^{(p)}) + \sin(\varphi_{D,az}^{(q)}) \cos(\varphi_{D,el}^{(q)}), \\ \psi_3^{(p,q)} &= \sin(\varphi_{A,el}^{(p)}) + \sin(\varphi_{D,el}^{(q)}). \end{aligned} \quad (15)$$

This paper assumes that  $K$  training subcarriers are provided among all  $K_0$  subcarriers. Without loss of generality, we further assume that the first  $K$  subcarriers (i.e.,  $k = 1, \dots, K$ ) are designed for pilot transmission for ease of exposition. The extension to the general case with equispaced training subcarriers is straightforward. We aim to extract unknown multipath parameters for UE-BS and UE-RIS-BS links to recover these two channels using received training signals. The parameters of interest are: delays  $\{\tau_L^{(\ell)}\} \cup \{\tau_R^{(p,q)}\}$ , angle-related parameters at RIS  $\{\psi_2^{(p,q)}, \psi_3^{(p,q)}\}$ , AOAs at BS  $\{\boldsymbol{\theta}_L^{(\ell)}\} \cup \{\boldsymbol{\theta}_R^{(q)}\}$ , and path gains  $\{\beta_L^{(\ell)}\} \cup \{\beta_R^{(p,q)}\}$ . Note that  $\{\psi_2^{(p,q)}, \psi_3^{(p,q)}\}$  are generated from the cascaded UE-RIS-BS channel and not related to the direct UE-BS link. In addition,  $\{\boldsymbol{\theta}_R^{(q)}\}$  merely come from the RIS-BS channel, irrelevant to the UE-RIS one. These two findings will be leveraged in the following algorithm development presented in the next section.

Some discussions on our UAV-mounted RIS scenario can be found in the sequel. In traditional cases with fixed RIS deployed on walls, roadsides, etc., the CSI for RIS-BS link can be accurately measured in advance, serving as prior information to simplify the estimation of other channels [34]. Nevertheless, this paper discusses a general CE case without any RIS-related information known a priori as the result of the agile state of UAV-mounted RIS. Reversely, with the recovery of channel parameters, we can further determine

the RIS state (e.g., location and orientation) [35]. From the system design aspect, the customizable state of UAV-mounted RIS also provides additional degree of freedoms (DOFs) in optimizing system performances.

### III. PROPOSED TENSOR-BASED CE FRAMEWORK

#### A. Tensor Construction

Our CE framework is developed under a noise-free model to illuminate its rationale. In real-world cases, the noise-free signal should be replaced by noisy observation as the algorithm input. We define from (10) that  $\mathbf{y}_L^{(k,g)} = \mathbf{R}^H \mathbf{h}_L^{(k)} x^{(k,g)} \in \mathbb{C}^{N_1 N_2 \times 1}$  and  $\mathbf{y}_R^{(k,g)} = \mathbf{R}^H \mathbf{h}_R^{(k,g)} x^{(k,g)}$  represent the noise-free received signals traveled from direct and cascaded channels, respectively. Vertically stack  $\mathbf{y}_L^{(k,g)}$  and  $\mathbf{y}_R^{(k,g)}$  over time slot  $g$ 's, respectively, yielding

$$\mathbf{y}_L^{(k)} = \sum_{\ell=1}^L \beta_L^{(\ell)} e^{-j2\pi f^{(k)} \tau_L^{(\ell)}} (\mathbf{x}^{(k)}) \otimes (\mathbf{R}^H \mathbf{a}_B(\boldsymbol{\theta}_L^{(\ell)})), \quad (16)$$

$$\begin{aligned} \mathbf{y}_R^{(k)} &= \sum_{p=1}^P \sum_{q=1}^Q \beta_R^{(p,q)} e^{-j2\pi f^{(k)} \tau_R^{(p,q)}} \left( \text{diag}(\mathbf{x}^{(k)}) \boldsymbol{\Upsilon} \right. \\ &\quad \left. \times (\mathbf{a}^{(M_y)}(\omega_2^{(p,q)}) \otimes \mathbf{a}^{(M_z)}(\omega_3^{(p,q)})) \right) \otimes (\mathbf{R}^H \mathbf{a}_B(\boldsymbol{\theta}_R^{(q)})), \end{aligned}$$

where  $\mathbf{y}_{L(R)}^{(k)} = [\mathbf{y}_{L(R)}^{(k,1)}, \dots, \mathbf{y}_{L(R)}^{(k,G)}]^T \in \mathbb{C}^{G N_1 N_2 \times 1}$ ,  $\mathbf{x}^{(k)} = [x^{(k,1)}, \dots, x^{(k,G)}]^T \in \mathbb{C}^{G \times 1}$  denotes the pilot collection for the  $k$ th subcarrier, and  $\boldsymbol{\Upsilon} = [\boldsymbol{\gamma}^{(1)}, \dots, \boldsymbol{\gamma}^{(G)}]^T \in \mathbb{C}^{G \times M_y M_z}$  is the RIS profile matrix over all time slots.

We customize the transmission pilots, RIS profile, the combining matrix to facilitate channel estimation. Firstly, identical pilots are selected across slots and training subcarriers, i.e.,  $x^{(k,g)} = x^{(k',g')}$ ,  $k, k' \in \{1, \dots, K\}$ ,  $g, g' \in \{1, \dots, G\}$ , and thus omit the superscripts of pilot notations hereafter. In this case, it is true that

$$\mathbf{x} = \mathbf{x} \mathbf{1}_{G \times 1} = (\sqrt{x} \mathbf{1}_{G_1 \times 1}) \otimes (\sqrt{x} \mathbf{1}_{G_2 \times 1}), \quad (17)$$

with  $G = G_1 G_2$ . Secondly, we design

$$\text{diag}(\mathbf{x}) \boldsymbol{\Upsilon} = \mathbf{x} \boldsymbol{\Upsilon} = \mathbf{T}_2^H \otimes \mathbf{T}_3^H, \quad (18)$$

with carefully preset Vandermonde matrices  $\mathbf{T}_2 \in \mathbb{C}^{M_y \times G_1}$  and  $\mathbf{T}_3 \in \mathbb{C}^{M_z \times G_2}$ . The solution of RIS profile matrix  $\boldsymbol{\Upsilon}$  lies in  $\boldsymbol{\Upsilon} = \frac{1}{x} \mathbf{T}_2^H \otimes \mathbf{T}_3^H$ . Thirdly, the combining matrix is set as

$$\mathbf{R} = \mathbf{T}_4 \otimes \mathbf{T}_5, \quad (19)$$

where  $\mathbf{T}_4 \in \mathbb{C}^{\tilde{N}_y \times N_1}$  and  $\mathbf{T}_5 \in \mathbb{C}^{\tilde{N}_z \times N_2}$  are also pre-constructed Vandermonde matrices. The special structure of  $\{\mathbf{T}_n\}_{n=2}^5$  will be utilized in Sections III-B and III-D.

With the designs above, further vertically collecting  $\mathbf{y}_L^{(k)}$  and  $\mathbf{y}_R^{(k)}$  in (16) across training subcarrier  $k$ 's, respectively, it follows that

$$\mathbf{y}_L = \sum_{\ell=1}^L \beta_L^{(\ell)} (\mathbf{a}^{(K)}(\omega_{1,L}^{(\ell)})) \otimes (\sqrt{x} \mathbf{1}_{G_1 \times 1}) \quad (20)$$

$$\begin{aligned} &\otimes (\sqrt{x} \mathbf{1}_{G_2 \times 1}) \otimes (\mathbf{T}_4^H \mathbf{a}^{(\tilde{N}_y)}(\omega_{4,L}^{(\ell)})) \otimes (\mathbf{T}_5^H \mathbf{a}^{(\tilde{N}_z)}(\omega_{5,L}^{(\ell)})), \\ \mathbf{y}_R &= \sum_{p=1}^P \sum_{q=1}^Q \beta_R^{(p,q)} (\mathbf{a}^{(K)}(\omega_{1,R}^{(p,q)})) \otimes (\mathbf{T}_2^H \mathbf{a}^{(M_y)}(\omega_2^{(p,q)})) \\ &\otimes (\mathbf{T}_3^H \mathbf{a}^{(M_z)}(\omega_3^{(p,q)})) \otimes (\mathbf{T}_4^H \mathbf{a}^{(\tilde{N}_y)}(\omega_{4,R}^{(q)})) \otimes (\mathbf{T}_5^H \mathbf{a}^{(\tilde{N}_z)}(\omega_{5,R}^{(q)})), \end{aligned}$$

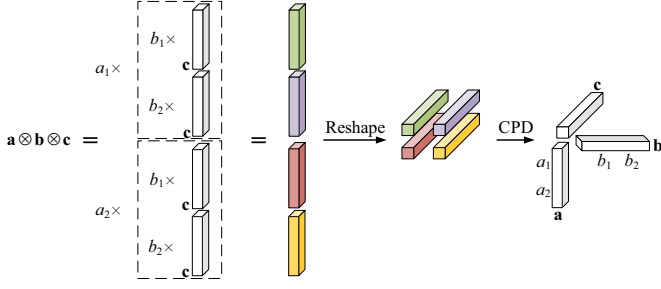


Fig. 2. Illustration of reshaping Kronecker product of vectors into a tensor. We consider an example with  $\mathbf{a} \otimes \mathbf{b} \otimes \mathbf{c}$  resulting in a third-order rank-1 tensor, where both  $\mathbf{a}$  and  $\mathbf{b}$  only contain two elements for ease of illustration.

where we have capitalized on (8) and added individual subscripts and superscripts,  $\mathbf{y}_L, \mathbf{y}_R \in \mathbb{C}^{K G_1 G_2 N_1 N_2 \times 1}$ , and

$$\omega_{1,L}^{(\ell)} = -2\pi \Delta_f \tau_L^{(\ell)}, \quad \omega_{1,R}^{(p,q)} = -2\pi \Delta_f \tau_R^{(p,q)}. \quad (21)$$

Reshape  $\mathbf{y}_L$  and  $\mathbf{y}_R$  in (20) into corresponding tensors  $\mathcal{Y}_L, \mathcal{Y}_R \in \mathbb{C}^{K \times G_1 \times G_2 \times N_1 \times N_2}$  and let  $\mathcal{Y} = \mathcal{Y}_L + \mathcal{Y}_R$ , yielding

$$\mathcal{Y} = \llbracket \beta; \mathbf{A}_1, \mathbf{B}_2, \mathbf{B}_3, \mathbf{B}_4, \mathbf{B}_5 \rrbracket, \quad (22)$$

where the weight vector  $\beta$  and factor matrices  $\mathbf{A}_1, \mathbf{B}_2, \dots, \mathbf{B}_5$  are given in (23)–(28) shown at the bottom of this page, and let  $R = L + C$  be the overall number of paths or, equivalently, the tensor rank with path number  $C = PQ$  of the cascaded UE-RIS-BS channel. The process of converting the Kronecker product of vectors into a tensor is illustrated in Fig. 2. Let  $\mathbf{B}_n = [\sqrt{x} \mathbf{1}_{1 \times L} \otimes \mathbf{1}_{G_{n-1} \times 1}, \mathbf{T}_n^H \mathbf{A}_n], n = 2, 3$  and  $\mathbf{B}_n = \mathbf{T}_n^H \mathbf{A}_n, n = 4, 5$ . Note that  $\{\mathbf{A}_n\}_{n=1}^5$  are all Vandermonde matrices, but generally  $\mathbf{A}_1$  is the merely Vandermonde CP factor of  $\mathcal{Y}$  regardless of  $\{\mathbf{T}_n\}_{n=2}^5$ . In the noisy case, the received signal tensor is  $\hat{\mathcal{Y}} = \mathcal{Y} + \mathcal{W}$  with noise tensor  $\mathcal{W}$ .

We analyze the CPD uniqueness of tensor  $\mathcal{Y}$  concerning the classical Kruskal condition [36, Section 3.2]. Since  $\mathbf{A}_1$  is generally a full-rank Vandermonde matrix with distinct generators  $\{\omega_{1,L}^{(\ell)}\} \cup \{\omega_{1,R}^{(p,q)}\}$ ,  $k_{\mathbf{A}_1} = \text{rank}(\mathbf{A}_1) = \min(K, R)$ . Nevertheless, all the other factors  $\{\mathbf{B}_n\}_{n=2}^5$  have repeated columns in the multipath scenario (i.e.,  $L, P, Q \geq 2$ ), thus  $k_{\mathbf{B}_n} = 1, n = 2, 3, 4, 5$ . As such, the Kruskal condition for CPD uniqueness can not be satisfied, and hence, the direct CPD for  $\mathcal{Y}$  is inapplicable. To overcome the rank-deficient issue, spatial smoothing and VSCPD techniques will

be employed to relax the uniqueness condition and acquire factor matrices.

### B. ESPRIT Preliminaries

We briefly discuss estimation of signal parameters via rotational invariance techniques (ESPRIT) type mechanisms. The reader is referred to [29, Section III-B] for a detailed summary. ESPRIT provides an algebraic solution of generator  $\omega$  of Vandermonde matrix  $\mathbf{A}$ . There are two estimation models: the element-space model and the transformed-space model. In the element-space model,  $\mathbf{A}$  inherently has the shift-invariance property  $\mathbf{J}^\dagger \mathbf{A} \text{diag}(\omega) = \mathbf{J}^\dagger \mathbf{A}$  with selection matrices  $\{\mathbf{J}^\dagger, \mathbf{J}^\downarrow\}$ . Once we obtain  $\hat{\mathbf{A}}$  satisfying  $\mathbf{A} = \hat{\mathbf{A}} \mathbf{D}$  with non-singular matrix  $\mathbf{D}$ ,  $\omega$  and  $\mathbf{D}$  can be recovered from the eigenvalue decomposition (EVD) of  $(\mathbf{J}^\dagger \hat{\mathbf{A}})^\dagger \mathbf{J}^\downarrow \hat{\mathbf{A}}$ . In the transformed-space (e.g., beamspace) model, the signal subspace of  $\mathbf{A}$  is converted via  $\mathbf{B} = \mathbf{T}^H \mathbf{A}$  with transformation matrix  $\mathbf{T}$ . Also, we can only acquire  $\hat{\mathbf{B}}$  with  $\mathbf{B} = \hat{\mathbf{B}} \mathbf{D}$ . The profound works in [37], [38] have shown that we have similar shift-invariance property  $\mathbf{Q} \mathbf{B} \text{diag}(\omega) = \mathbf{Q} \mathbf{F}^H \mathbf{B}$  via preset projection matrix  $\mathbf{Q}$  and Vandermonde matrix  $\mathbf{T}$  satisfying  $\mathbf{J}^\dagger \mathbf{T} = \mathbf{J}^\downarrow \mathbf{T} \mathbf{F}$ . Subsequently, we can acquire  $\omega$  and  $\mathbf{D}$  through the EVD of  $(\mathbf{Q} \hat{\mathbf{B}})^\dagger \mathbf{Q} \mathbf{F}^H \hat{\mathbf{B}}$ .

### C. VSCPD with Spatial Smoothing

The signal tensor is first augmented via spatial smoothing, depending on the Vandermonde structure. Since factor  $\mathbf{A}_1$  is the only Vandermonde factor, we employ spatial smoothing in mode 1, resulting in an extended signal tensor  $\mathcal{Y}_{\text{sps}} \in \mathbb{C}^{K_1 \times G_1 \times G_2 \times N_1 \times N_2 \times K_2}$  with  $K_1 + K_2 - 1 = K$ . The elements of  $\mathcal{Y}_{\text{sps}}$  are expressed as

$$\begin{aligned} [\mathcal{Y}_{\text{sps}}]_{k_1, g_1, g_2, n_1, n_2, k_2} &= [\mathcal{Y}]_{k_1 + k_2 - 1, g_1, g_2, n_1, n_2} \\ &= \sum_{r=1}^R [\beta]_r e^{-j2\pi(k_1-1)\Delta_f[\tau]_r} e^{-j2\pi(k_2-1)\Delta_f[\tau]_r} \\ &\quad \times [\mathbf{B}_2]_{g_1, r} [\mathbf{B}_3]_{g_2, r} [\mathbf{B}_4]_{n_1, r} [\mathbf{B}_5]_{n_2, r}, \end{aligned} \quad (29)$$

where  $\tau \in \mathbb{R}^{R \times 1}$  is the delay collection defined like (23). As such,  $\mathcal{Y}_{\text{sps}}$  can be expressed in CPD form as

$$\mathcal{Y}_{\text{sps}} = \llbracket \beta; \mathbf{B}_1, \mathbf{B}_2, \mathbf{B}_3, \mathbf{B}_4, \mathbf{B}_5, \mathbf{B}_6 \rrbracket, \quad (30)$$

where  $\mathbf{B}_n = \mathbf{T}_n^H \mathbf{A}_1, n = 1, 6$  with two selection matrices  $\mathbf{T}_1^H = [\mathbf{I}_{K_1}, \mathbf{0}_{K_1 \times (K-K_1)}] \in \mathbb{R}^{K_1 \times K}$  and  $\mathbf{T}_6^H =$

$$\beta = [\beta_L^{(1)}, \dots, \beta_L^{(L)}, \beta_R^{(1,1)}, \dots, \beta_R^{(P,Q)}]^T \in \mathbb{C}^{R \times 1}, \quad (23)$$

$$\mathbf{A}_1 = [\mathbf{a}^{(K)}(\omega_{1,L}^{(1)}), \dots, \mathbf{a}^{(K)}(\omega_{1,L}^{(L)}), \mathbf{a}^{(K)}(\omega_{1,R}^{(1)}), \dots, \mathbf{a}^{(K)}(\omega_{1,R}^{(P,Q)})] \in \mathbb{C}^{K \times R}, \quad (24)$$

$$\mathbf{B}_2 = \underbrace{[\sqrt{x} \mathbf{1}_{G_1 \times 1}, \dots, \sqrt{x} \mathbf{1}_{G_1 \times 1}]_L}_{L} \underbrace{[\mathbf{T}_2^H \mathbf{a}^{(M_y)}(\omega_2^{(1,1)}), \dots, \mathbf{T}_2^H \mathbf{a}^{(M_y)}(\omega_2^{(P,Q)})]_C}_{C} \in \mathbb{C}^{G_1 \times R}, \quad (25)$$

$$\mathbf{B}_3 = [\sqrt{x} \mathbf{1}_{G_2 \times 1}, \dots, \sqrt{x} \mathbf{1}_{G_2 \times 1}, \mathbf{T}_3^H \mathbf{a}^{(M_z)}(\omega_3^{(1,1)}), \dots, \mathbf{T}_3^H \mathbf{a}^{(M_z)}(\omega_3^{(P,Q)})] \in \mathbb{C}^{G_2 \times R}, \quad (26)$$

$$\mathbf{B}_4 = \mathbf{T}_4^H \underbrace{[\mathbf{a}^{(\tilde{N}_y)}(\omega_{4,L}^{(1)}), \dots, \mathbf{a}^{(\tilde{N}_y)}(\omega_{4,L}^{(L)})]_L}_{L} \underbrace{[\mathbf{a}^{(\tilde{N}_y)}(\omega_{4,R}^{(1)}), \dots, \mathbf{a}^{(\tilde{N}_y)}(\omega_{4,R}^{(1)})]_P}_{P} \underbrace{[\mathbf{a}^{(\tilde{N}_y)}(\omega_{4,R}^{(Q)}), \dots, \mathbf{a}^{(\tilde{N}_y)}(\omega_{4,R}^{(Q)})]_P}_{P} \in \mathbb{C}^{N_1 \times R}, \quad (27)$$

$$\mathbf{B}_5 = \mathbf{T}_5^H [\mathbf{a}^{(\tilde{N}_z)}(\omega_{5,L}^{(1)}), \dots, \mathbf{a}^{(\tilde{N}_z)}(\omega_{5,L}^{(L)}), \mathbf{a}^{(\tilde{N}_z)}(\omega_{5,R}^{(1)}), \dots, \mathbf{a}^{(\tilde{N}_z)}(\omega_{5,R}^{(1)}), \dots, \mathbf{a}^{(\tilde{N}_z)}(\omega_{5,R}^{(Q)}), \dots, \mathbf{a}^{(\tilde{N}_z)}(\omega_{5,R}^{(Q)})] \in \mathbb{C}^{N_2 \times R}. \quad (28)$$

$[\mathbf{I}_{K_2}, \mathbf{0}_{K_2 \times (K-K_2)}] \in \mathbb{R}^{K_2 \times K}$ . In the following, we give the general VSCPD uniqueness condition for a fifth-order tensor with only one Vandermonde factor. This is an extended version of [26, Theorem III.3] to a higher-order case.

*Theorem 1:* Let  $\mathbf{A}_1 \in \mathbb{C}^{K \times R}$ ,  $\mathbf{B}_2 \in \mathbb{C}^{G_1 \times R}$ ,  $\mathbf{B}_3 \in \mathbb{C}^{G_2 \times R}$ ,  $\mathbf{B}_4 \in \mathbb{C}^{N_1 \times R}$ , and  $\mathbf{B}_5 \in \mathbb{C}^{N_2 \times R}$  be the factor matrices of tensor  $\mathcal{Y} \in \mathbb{C}^{K \times G_1 \times G_2 \times N_1 \times N_2}$  with weight vector  $\beta$ , and  $\mathbf{A}_1$  is a Vandermonde matrix formed by distinct generators  $[\omega_1]_r, r = 1, \dots, R$ . Define  $\mathbf{B}_n = \mathbf{T}_n^H \mathbf{A}_1, n = 1, 6$ , where  $\mathbf{T}_1^H = [\mathbf{I}_{K_1}, \mathbf{0}_{K_1 \times (K-K_1)}]$  and  $\mathbf{T}_6^H = [\mathbf{I}_{K_2}, \mathbf{0}_{K_2 \times (K-K_2)}]$  with  $K_1 + K_2 - 1 = K$ . If

$$\begin{cases} \text{rank}(\underline{\mathbf{B}}_1 \odot \mathbf{B}_2 \odot \mathbf{B}_3) = R \\ \text{rank}(\mathbf{B}_4 \odot \mathbf{B}_5 \odot \mathbf{B}_6) = R, \end{cases} \quad (31)$$

then the VSCPD of  $\mathcal{Y}$  is said to be unique. Generically, (31) becomes

$$\min((K_1 - 1)G_1G_2, K_2N_1N_2) \geq R. \quad (32)$$

*Proof:* Following [39, Theorem 3], obtaining (32) from (31) is straightforward. Consequently, we only concentrate on the proof of (31). Consider the extended tensor  $\mathcal{Y}_{\text{sps}} = \llbracket \beta; \mathbf{B}_1, \mathbf{B}_2, \mathbf{B}_3, \mathbf{B}_4, \mathbf{B}_5, \mathbf{B}_6 \rrbracket \in \mathbb{C}^{K_1 \times G_1 \times G_2 \times N_1 \times N_2 \times K_2}$ . Denote the mode-3 matrix representation of  $\mathcal{Y}_{\text{sps}}$  by  $\mathbf{Y}_{\text{sps},[3]} \in \mathbb{C}^{K_1G_1G_2 \times N_1N_2K_2}$ , expressed as [26, Eq. (4)]

$$\mathbf{Y}_{\text{sps},[3]} = (\mathbf{B}_1 \odot \mathbf{B}_2 \odot \mathbf{B}_3) \text{diag}(\beta) (\mathbf{B}_4 \odot \mathbf{B}_5 \odot \mathbf{B}_6)^T. \quad (33)$$

Define two selection matrices

$$\begin{aligned} \mathbf{J}^\uparrow &= [\mathbf{I}_{K_1-1}, \mathbf{0}_{(K_1-1) \times 1}] \otimes \mathbf{I}_{G_1} \otimes \mathbf{I}_{G_2}, \\ \mathbf{J}^\downarrow &= [\mathbf{0}_{(K_1-1) \times 1}, \mathbf{I}_{K_1-1}] \otimes \mathbf{I}_{G_1} \otimes \mathbf{I}_{G_2}, \end{aligned} \quad (34)$$

then we come to

$$\begin{aligned} \mathbf{J}^\uparrow \mathbf{B}_{123} &= \underline{\mathbf{B}}_1 \odot \mathbf{B}_2 \odot \mathbf{B}_3, \\ \mathbf{J}^\downarrow \mathbf{B}_{123} &= (\underline{\mathbf{B}}_1 \odot \mathbf{B}_2 \odot \mathbf{B}_3) \text{diag}(\omega_1), \end{aligned} \quad (35)$$

with  $\mathbf{B}_{123} = \mathbf{B}_1 \odot \mathbf{B}_2 \odot \mathbf{B}_3$ , and thus

$$\mathbf{J}^\uparrow \mathbf{B}_{123} \text{diag}(\omega_1) = \mathbf{J}^\downarrow \mathbf{B}_{123}. \quad (36)$$

Given the conditions in (31), we have the full-rank property  $\text{rank}(\mathbf{B}_{123}) = R$ , and then following (33) we also have  $\text{rank}(\mathbf{Y}_{\text{sps},[3]}) = R$ . Let  $\mathbf{Y}_{\text{sps},[3]} = \mathbf{U}\Sigma\mathbf{V}^H$  be the compact singular value decomposition (SVD). Notice that  $\mathbf{B}_{123}$  and  $\mathbf{U}$  share the same signal subspace, hence

$$\mathbf{B}_{123} = \mathbf{U}\mathbf{D}, \quad \mathbf{B}_{456} = \mathbf{V}^*\Sigma\mathbf{D}^{-T} \text{diag}(\beta)^{-1}, \quad (37)$$

with  $\mathbf{B}_{456} = \mathbf{B}_4 \odot \mathbf{B}_5 \odot \mathbf{B}_6$  and non-singular matrix  $\mathbf{D}$ . Referring to Section III-B, we can utilize the EVD-based element-space ESPRIT to extract  $\omega_1$  and  $\mathbf{D}$ . Herein, (31) ensures the existence of  $(\mathbf{J}^\uparrow \mathbf{B}_{123})^\dagger$ . The ESPRIT results have permutation and scaling issues. i.e.,  $\hat{\omega}_1^T = \omega_1^T \mathbf{\Pi}$  and  $\hat{\mathbf{D}} = \mathbf{D} \text{diag}(\rho) \mathbf{\Pi}$  with permutation matrix  $\mathbf{\Pi}$  and scaling vector  $\rho$ . Further, using generators, we can construct  $\hat{\mathbf{B}}_1 = \mathbf{B}_1 \mathbf{\Pi}$  and  $\hat{\mathbf{B}}_6 = \mathbf{B}_6 \mathbf{\Pi}$ .

Denote the  $r$ th column of  $\mathbf{B}_n$  ( $\hat{\mathbf{B}}_n$ ) by  $\mathbf{b}_{n,r}$  ( $\hat{\mathbf{b}}_{n,r}$ ). Further let  $\mathbf{b}_{23,r} = \mathbf{b}_{2,r} \otimes \mathbf{b}_{3,r}$  and  $\mathbf{b}_{45,r} = \mathbf{b}_{4,r} \otimes \mathbf{b}_{5,r}$ . We have

$$\begin{aligned} \mathbf{b}_{23,r} &= K_1^{-1} (\hat{\mathbf{b}}_{1,r}^H \otimes \mathbf{I}_{G_1G_2}) (\hat{\mathbf{b}}_{1,r} \otimes \mathbf{b}_{23,r}), \\ \mathbf{b}_{45,r} &= K_2^{-1} (\mathbf{I}_{N_1N_2} \otimes \hat{\mathbf{b}}_{6,r}^H) (\mathbf{b}_{45,r} \otimes \hat{\mathbf{b}}_{6,r}), \end{aligned} \quad (38)$$

$$\hat{\mathbf{b}}_{1,r} \otimes \mathbf{b}_{23,r} = [\rho]_r^{-1} \mathbf{U} \hat{\mathbf{d}}_r, \quad \mathbf{b}_{45,r} \otimes \hat{\mathbf{b}}_{6,r} = [\beta]_r^{-1} [\rho]_r \mathbf{V}^* \hat{\Sigma} \hat{\mathbf{d}}_r,$$

---

### Algorithm 1 VSCPD with spatial smoothing.

---

**Input:** Tensor  $\hat{\mathcal{Y}}$  in the noisy case and rank  $R$ .

**Implementation:**

- 1: Apply spatial smoothing using (29) to form  $\hat{\mathcal{Y}}_{\text{sps}}$ .
  - 2: Construct mode-3 matrix representation  $\hat{\mathbf{Y}}_{\text{sps},[3]}$ .
  - 3: Calculate compact CPD  $\hat{\mathbf{Y}}_{\text{sps},[3]} = \mathbf{U}\Sigma\mathbf{V}^H$ .
  - 4: Compute selection matrices  $\mathbf{J}^\uparrow$  and  $\mathbf{J}^\downarrow$  using (34).
  - 5: Leverage  $\{\mathbf{U}, \mathbf{J}^\uparrow, \mathbf{J}^\downarrow\}$  to acquire  $\{\hat{\omega}, \hat{\mathbf{D}}\}$  using ESPRIT.
  - 6: **for**  $r = 1$  to  $R$  **do**
  - 7: Utilize generator  $[\hat{\omega}_1]_r$  to construct  $\hat{\mathbf{b}}_{n,r}, n = 1, 6$ .
  - 8: Calculate SVD of  $\text{unvec}_{G_2 \times G_1}((\hat{\mathbf{b}}_{1,r}^H \otimes \mathbf{I}_{G_1G_2}) \mathbf{U} \hat{\mathbf{d}}_r)$  to obtain  $\hat{\mathbf{b}}_{n,r}, n = 2, 3$ .
  - 9: Compute SVD of  $\text{unvec}_{N_2 \times N_1}((\mathbf{I}_{N_1N_2} \otimes \hat{\mathbf{b}}_{6,r}^H) \mathbf{V}^* \hat{\Sigma} \hat{\mathbf{d}}_r)$  to get  $\hat{\mathbf{b}}_{n,r}, n = 4, 5$ .
  - 10: **end for**
- Output:** Factors  $\{\hat{\mathbf{B}}_n\}_{n=1}^6$  and generator  $\hat{\omega}_1$ .
- 

where  $\hat{\mathbf{d}}_r$  ( $\hat{\mathbf{d}}_r$ ) is the  $r$ th column of  $\hat{\mathbf{D}}$  ( $\hat{\mathbf{D}}^{-T}$ ). With (38) at hand, we can solve  $\{\hat{\mathbf{b}}_{2,r}, \hat{\mathbf{b}}_{3,r}\}$  and  $\{\hat{\mathbf{b}}_{4,r}, \hat{\mathbf{b}}_{5,r}\}$  via rank-1 approximation, i.e.,

$$\begin{aligned} \min_{\hat{\mathbf{b}}_{2,r}, \hat{\mathbf{b}}_{3,r}} & \left\| K_1 \hat{\mathbf{b}}_{3,r} \hat{\mathbf{b}}_{2,r}^H - \text{unvec}_{G_2 \times G_1}((\hat{\mathbf{b}}_{1,r}^H \otimes \mathbf{I}_{G_1G_2}) \mathbf{U} \hat{\mathbf{d}}_r) \right\|_F^2, \\ \min_{\hat{\mathbf{b}}_{4,r}, \hat{\mathbf{b}}_{5,r}} & \left\| K_2 \hat{\mathbf{b}}_{5,r} \hat{\mathbf{b}}_{4,r}^H - \text{unvec}_{N_2 \times N_1}((\mathbf{I}_{N_1N_2} \otimes \hat{\mathbf{b}}_{6,r}^H) \mathbf{V}^* \hat{\Sigma} \hat{\mathbf{d}}_r) \right\|_F^2. \end{aligned}$$

SVD can solve the problems above, and the results of  $\hat{\mathbf{b}}_{3(5),r}$  and  $\hat{\mathbf{b}}_{2(4),r}$  are the left and right singular vectors of the second term inside the norm, respectively. ■

The implementation of VSCPD with spatial smoothing is outlined in Algorithm 1. Importantly, our approach utilizes only standard linear algebra and avoids initialization and iterations by leveraging the power of the Vandermonde structure. Like other CPD techniques, VSCPD results still have permutation and scaling problems.

With Theorem 1, we analyze the VSCPD uniqueness condition of our case with factor matrices shown in (24)–(28). We have  $k_{\underline{\mathbf{B}}_1} = \text{rank}(\underline{\mathbf{B}}_1) = \min(K_1 - 1, R)$  with distinct generators in general. Recall that  $k_{\mathbf{B}_2} = k_{\mathbf{B}_3} = 1$  due to redundant columns in multipath scenario. For matrices  $\{\mathbf{X}, \mathbf{Y}\}$  both having  $R$  columns, we find [39]

$$\text{rank}(\mathbf{X} \odot \mathbf{Y}) \geq k_{\mathbf{X} \odot \mathbf{Y}} \geq \min(k_{\mathbf{X}} + k_{\mathbf{Y}} - 1, R). \quad (39)$$

Based on this property,  $\text{rank}(\underline{\mathbf{B}}_1 \odot \mathbf{B}_2 \odot \mathbf{B}_3) = \min(K_1 - 1, R)$ . To fulfill the first condition in (31), it is necessary that  $K_1 - 1 \geq R$ . Similarly, to satisfy the second condition in (31), it is necessary that  $K_2 \geq R$ . In summary, the VSCPD is unique if

$$\min(K_1 - 1, K_2) \geq R, \quad (40)$$

depending solely on spatial smoothing parameters  $\{K_1, K_2\}$  with given  $R$ . Importantly, (40) provides a far more relaxed CPD uniqueness condition than the classical Kruskal one. With  $K_1 + K_2 - 1 = K$ , the training subcarrier number should be set as  $K \geq 2R$ .

The following subsections develop a triple-stage CE framework with factor estimates as input. Stage I performs

---

**Algorithm 2** Algebraic CE algorithm (Stage I).
 

---

**Input:** Factor columns  $\{\hat{\mathbf{b}}_{n,r}\}$ , generator  $\hat{\omega}_1$ , and path numbers  $\{L, P, Q\}$ .

**Implementation:**

- 1: Determine  $\hat{\mathcal{L}}_n, n \in \{2, 3\}$  based on *variance principle*.
- 2: **if**  $\hat{\mathcal{L}}_2 \neq \hat{\mathcal{L}}_3$  **then**
- 3:   Algorithm fails and **break**.
- 4: **else**
- 5:   Let  $\hat{\mathcal{L}} = \hat{\mathcal{L}}_2$  and determine its supplement  $\hat{\mathcal{C}} = \mathcal{R} \setminus \hat{\mathcal{L}}$ .
- 6:   Find  $\{\hat{\mathcal{P}}_n^{(\hat{q})}\}_{\hat{q}=1}^Q, n \in \{4, 5\}$  using *similarity principle*.
- 7:   **if**  $\hat{\mathcal{P}}_4^{(\hat{q})} \neq \hat{\mathcal{P}}_5^{(\hat{q})}, \exists \hat{q} \in \mathcal{Q}$  **then**
- 8:     Algorithm fails and **break**.
- 9:   **else**
- 10:     Let  $\hat{\mathcal{P}}^{(\hat{q})} = \hat{\mathcal{P}}_4^{(\hat{q})}$ .
- 11:     **for**  $r \in \hat{\mathcal{C}}$  if  $n \in \{2, 3\}$  **or**  $r \in \mathcal{R}$  if  $n \in \{4, 5\}$  **do**
- 12:       Calculate  $\hat{\omega}_{n,r}$  for each  $n$  using (42).
- 13:     **end for**
- 14:     Recover multipath parameters using (43)–(46).
- 15:   **end if**
- 16: **end if**

**Output:** Channel-parameter estimates and sets  $\{\hat{\mathcal{L}}, \hat{\mathcal{C}}, \hat{\mathcal{P}}^{(\hat{q})}\}$ .

---

multipath identification and coarse estimation. Subsequently, Stages II and III serve as optional double refinements at the cost of complexity growth.

#### D. CE Stage I for Path Identification and Coarse Estimation

Firstly, multipath identification is performed for different physical groups. Define  $\mathcal{R} = \{1, \dots, R\}$ ,  $\mathcal{L} = \{1, \dots, L\}$ ,  $\mathcal{P} = \{1, \dots, P\}$ , and  $\mathcal{Q} = \{1, \dots, Q\}$ .

Recall that  $\{\psi_2^{(p,q)}, \psi_3^{(p,q)}\}$  are only related to the cascaded UE-RIS-BS channel; thus we have to distinguish cascaded UE-RIS-BS paths from direct UE-BS paths. Thanks to our unique pilot design, (25) shows that the columns corresponding to direct UE-BS paths in  $\mathbf{B}_2$  have the minimal  $L$  variances. The same is true for  $\mathbf{B}_3$  in (26). Therefore, we can deduce from  $\{\hat{\mathbf{b}}_{2(3),r}\}_{r=1}^R$  an index set  $\hat{\mathcal{L}}_{2(3)}$  for direct paths, associated with  $L$  lowest variance. This strategy is referred to as the *variance principle*, and here  $\hat{\mathcal{L}}_n \subset \mathcal{R}$  with cardinality  $\text{card}(\hat{\mathcal{L}}_n) = L$  for each  $n \in \{2, 3\}$ . At this moment, our pilot setting provides a chance to judge the algorithm status regarding tensor decomposition. In the successful decomposition case, we should have  $\hat{\mathcal{L}}_2 = \hat{\mathcal{L}}_3$ ; otherwise, if  $\hat{\mathcal{L}}_2 \neq \hat{\mathcal{L}}_3$  holds, algorithm fails and thus procedure aborts here. To proceed, we will continue discussing the CE process for successful cases. Let  $\hat{\mathcal{L}} = \hat{\mathcal{L}}_2$ , and obtain the supplement  $\hat{\mathcal{C}} = \mathcal{R} \setminus \hat{\mathcal{L}}$  as the index set for cascaded paths with  $\text{card}(\hat{\mathcal{C}}) = C$ .

Further remind that  $\{\theta_R^{(q)}\}$  solely come from the RIS-BS channel. Owing to the cascaded channel characteristic, each  $\omega_{4(5),R}^{(q)}$  originated from  $\theta_R^{(q)}$ , generates  $P$  duplicate columns in  $\mathbf{B}_{4(5)}$  (see (27)–(28)). We hence aim to identify the cascaded paths formed by each RIS-BS sub-path using  $\{\hat{\mathbf{b}}_{n,r}\}_{r \in \hat{\mathcal{C}}}, n \in \{4, 5\}$ . We define the correlation-based similarity criterion, i.e.,

$$\text{sim}(\hat{\mathbf{b}}_{n,r}, \hat{\mathbf{b}}_{n,r'}) = \frac{|\hat{\mathbf{b}}_{n,r}^H \hat{\mathbf{b}}_{n,r'}|}{\|\hat{\mathbf{b}}_{n,r}\| \|\hat{\mathbf{b}}_{n,r'}\|}, \quad r \neq r' \in \hat{\mathcal{C}}. \quad (41)$$

With such a tool, we can group  $P$  paths that are similar enough to each other for  $Q$  times, called *similarity principle*. That is, we obtain from  $\{\hat{\mathbf{b}}_{4(5),r}\}_{r \in \hat{\mathcal{C}}}$  an index set  $\hat{\mathcal{P}}_{4(5)}^{(\hat{q})}$  for each RIS-BS sub-path,  $\hat{q} \in \mathcal{Q}$ . Herein,  $\text{card}(\hat{\mathcal{P}}_n^{(\hat{q})}) = P$  and  $\hat{\mathcal{P}}_n^{(1)} \cup \dots \cup \hat{\mathcal{P}}_n^{(Q)} = \hat{\mathcal{C}}$  for every  $n \in \{4, 5\}$ . Again, we can determine the algorithm status here thanks to channel nature. If  $\hat{\mathcal{P}}_4^{(\hat{q})} = \hat{\mathcal{P}}_5^{(\hat{q})}, \forall \hat{q} \in \mathcal{Q}$ , tensor decomposition succeeds; otherwise the procedure breaks at this point. We continue presenting the subsequence in successful cases and let  $\hat{\mathcal{P}}^{(\hat{q})} = \hat{\mathcal{P}}_4^{(\hat{q})}$ .

Using  $\{\hat{\mathbf{b}}_{n,r}\}$ , we utilize the transformed-space ESRPIT introduced in Section III-B to recover generators in modes 2–5. Nevertheless, instead of jointly calculating all generators like Section III-B in each mode, the column-wise scheme [37] is leveraged, helping with the parameter association along different modes. That is,

$$\hat{\omega}_{n,r} = (\mathbf{Q}_n \hat{\mathbf{b}}_{n,r})^\dagger \mathbf{Q}_n \mathbf{F}_n^H \hat{\mathbf{b}}_{n,r}, \quad \begin{cases} r \in \hat{\mathcal{C}}, & \text{if } n \in \{2, 3\}, \\ r \in \mathcal{R}, & \text{if } n \in \{4, 5\}. \end{cases} \quad (42)$$

The channel-parameter estimators using generator estimates are presented as follows. The VSCPD outputs  $\hat{\omega}_1$ , and let  $\hat{\omega}_{1,r} = [\hat{\omega}_1]_r, r \in \mathcal{R}$ . The delay estimates are expressed as

$$\hat{\tau}_r = -\frac{\hat{\omega}_{1,r}}{2\pi\Delta_f}, \quad r \in \mathcal{R}. \quad (43)$$

Then we conduct the element-wise mapping such that  $\hat{\tau}_r \mapsto \hat{\tau}_L^{(\hat{\ell})}, r \in \hat{\mathcal{L}}, \hat{\ell} \in \mathcal{L}$  and  $\hat{\tau}_r \mapsto \hat{\tau}_R^{(\hat{p}, \hat{q})}, r \in \hat{\mathcal{C}}, \hat{p} \in \mathcal{P}, \hat{q} \in \mathcal{Q}$ . In addition, we recover RIS's angle-related parameters from

$$\hat{\psi}_{n,r} = \frac{\lambda}{2\pi d_R} \hat{\omega}_{n,r}, \quad n = 2, 3, r \in \hat{\mathcal{C}}. \quad (44)$$

The mapping lies in  $\hat{\psi}_{1(2),r} \mapsto \hat{\psi}_{1(2)}^{(\hat{p}, \hat{q})}, r \in \hat{\mathcal{C}}, \hat{p} \in \mathcal{P}, \hat{q} \in \mathcal{Q}$ . Moreover, we acquire AOAs via

$$\hat{\theta}_{\text{el},r} = \arcsin\left(\frac{\lambda \hat{\omega}_{4,r}}{2\pi d_B}\right), \quad \hat{\theta}_{\text{az},r} = \arcsin\left(\frac{\lambda \hat{\omega}_{3,r}}{2\pi d_B \cos(\hat{\theta}_{\text{el},r})}\right). \quad (45)$$

We then map such that  $\hat{\theta}_{\text{az}(\text{el}),r} \mapsto \hat{\theta}_{L,\text{az}(\text{el})}^{(\hat{\ell})}, r \in \hat{\mathcal{L}}, \hat{\ell} \in \mathcal{L}$  and  $\frac{1}{P} \sum_{r \in \hat{\mathcal{P}}^{(\hat{q})}} \hat{\theta}_{\text{az}(\text{el}),r} \mapsto \hat{\theta}_{R,\text{az}(\text{el})}^{(\hat{q})}, \hat{q} \in \mathcal{Q}$ . Finally, we utilize  $\{\hat{\omega}_{n,r}\}$  to construct factor estimates  $\{\hat{\mathbf{B}}_n\}_{n=1}^6$ . The path gains can be estimated via [36, Eq. (2.2)]

$$\hat{\beta} = \mathbf{E} (\hat{\mathbf{B}}_6 \odot \hat{\mathbf{B}}_5 \odot \dots \odot \hat{\mathbf{B}}_2 \odot \hat{\mathbf{B}}_1)^H \text{vec}(\mathcal{Y}_{\text{sps}}), \quad \mathbf{E} = ((\hat{\mathbf{B}}_1^H \hat{\mathbf{B}}_1) \otimes (\hat{\mathbf{B}}_2^H \hat{\mathbf{B}}_2) \otimes \dots \otimes (\hat{\mathbf{B}}_6^H \hat{\mathbf{B}}_6))^\dagger. \quad (46)$$

Let  $[\hat{\beta}]_r = \hat{\beta}_r, r \in \mathcal{R}$ . We map that  $\hat{\beta}_r \mapsto \hat{\beta}_L^{(\hat{\ell})}, r \in \hat{\mathcal{L}}, \hat{\ell} \in \mathcal{L}$  and  $\hat{\beta}_r \mapsto \hat{\beta}_R^{(\hat{p}, \hat{q})}, r \in \hat{\mathcal{C}}, \hat{p} \in \mathcal{P}, \hat{q} \in \mathcal{Q}$ . Algorithm 2 concludes our CE algorithm in Stage I.

We have treated the path numbers  $\{R, L, P, Q\}$  as known values. In the case without such prior information, we can also estimate these path numbers under our framework. First,  $\hat{R}$  can be determined by the minimum description length (MDL) technique [40]. Further, in  $\{\hat{\mathbf{b}}_{2(3),r}\}_{r=1}^{\hat{R}}$ , the lowest  $L$  variances should be much smaller than the lowest  $(L+1)$ th one; based on such result, we can extend our *variance principle* to obtain  $\hat{L}$ . Analogously,  $\{\hat{P}, \hat{Q}\}$  can be also inferred using the extended *similarity principle*.

**Algorithm 3** Search-based CE refinement algorithm (Stage II).

**Input:** Coarse parameter estimates, factors  $\{\hat{\mathbf{B}}_n\}_{n=2}^5$ , matrices  $\{\mathbf{T}_n\}_{n=2}^5$ , index sets  $\{\hat{\mathcal{L}}, \hat{\mathcal{C}}, \hat{\mathcal{P}}^{(\hat{q})}\}$ , and search parameters  $\{\Delta_n^1, E_n, I_n, \zeta_n\}_{n=2}^5$ .

**Implementation:**

```

1: for  $n \in \{2, 3, 4, 5\}$  do
2:   for  $r \in \hat{\mathcal{C}}$  if  $n \in \{2, 3\}$  or  $r \in \mathcal{R}$  if  $n \in \{4, 5\}$  do
3:     for  $i = 1$  to  $I_n$  do
4:       Construct search space  $\mathcal{D}_{n,r}^i$  using (48).
5:       Search in  $\mathcal{D}_{n,r}^i$  to find a  $\hat{\omega}_{n,r}$  maximizing (47).
6:       Update search resolution  $\Delta_n^i$  using (49).
7:     end for
8:   end for
9: end for
10: Obtain multipath parameters using (44)–(46).
Output: Refined Channel-parameter estimates.

```

*E. CE Stage II for Estimate Refinement*

Although Stage I provides an ESPRIT-based algebraic solution with fast implementation, its output is not accurate enough [29]. To remedy this, we apply the correlation-based search (CBS) to improve the accuracy. Specifically, the optimization problem for only one variable is given by

$$\max_{\hat{\omega}_{n,r}} \frac{|\hat{\mathbf{b}}_{n,r}^H \mathbf{b}(\hat{\omega}_{n,r})|}{\|\hat{\mathbf{b}}_{n,r}\| \|\mathbf{b}(\hat{\omega}_{n,r})\|}, \begin{cases} r \in \hat{\mathcal{C}}, & \text{if } n \in \{2, 3\}, \\ r \in \mathcal{R}, & \text{if } n \in \{4, 5\}, \end{cases} \quad (47)$$

where  $\mathbf{b}(\hat{\omega}_{n,r}) = \mathbf{T}_n^H \mathbf{a}^{(X)}(\hat{\omega}_{n,r})$ ,  $X \in \{M_y, M_z, \tilde{N}_y, \tilde{N}_z\}$  corresponding to each  $n \in \{2, 3, 4, 5\}$ . Per [41, Appendix A], the CBS scheme is equivalent to the maximum likelihood (ML) estimator provided that the estimation error of  $\hat{\mathbf{b}}_{n,r}$  follows the circularly symmetric Gaussian distribution. Nonetheless, instead of searching exhaustively to solve (47) like [24], [25], [41], the following iterative search strategy is developed here. Let  $\Delta_n^i$ ,  $n \in \{2, 3, 4, 5\}$  be the  $i$ th search resolution,  $i = 1, \dots, I_n$ . Further, let  $\mathcal{D}_{n,r}^i$  denote the  $i$ th search space centered at the estimate obtained from the last iteration (input the estimate obtained in Stage I as the initial value). That is,  $\mathcal{D}_{n,r}^i$  is constructed from

$$\mathcal{D}_{n,r}^i = \{\dots, \hat{\omega}_{n,r}^{i-1} - \Delta_n^i, \hat{\omega}_{n,r}^{i-1}, \hat{\omega}_{n,r}^{i-1} + \Delta_n^i, \dots\}. \quad (48)$$

We fix the cardinality  $\text{card}(\mathcal{D}_{n,r}^i) = E_n$ . During each iteration, search in  $\mathcal{D}_{n,r}^i$  and output the estimate maximizing (47). Then resolution  $\Delta_n^i$  is shrunk in the following manner

$$\Delta_n^{i+1} = \zeta_n \Delta_n^i, \quad i = 1, \dots, I_n - 1, \quad (49)$$

with coefficient  $0 < \zeta_n < 1$ . Repeating the iteration  $I_n$  times yields CBS-refined estimates  $\{\hat{\omega}_{n,r}\}$ .

Subsequently, the updated  $\{\hat{\omega}_{n,r}\}$  can be used to reconstruct channel parameters (except delays) with better accuracy via (44)–(46). Algorithm 3 summarizes our CE Stage II.

*F. CE Stage III for Further Refinement*

The factor matrix estimates obtained in Stage II deliver a reliable CPD result. Such result can be then used as the initialization for the iterative ALS algorithm to produce more

**Algorithm 4** Iterative CE refinement algorithm (Stage III).

**Input:** Coarse factor estimates, noisy tensor  $\hat{\mathcal{Y}}_{\text{sps}}$ , maximum iteration number  $I_{\text{max}}$ , and convergence threshold  $\epsilon$ .

**Implementation:**

```

1: Let  $\hat{\mathcal{Y}}_{\text{sps}}^0 = \hat{\mathcal{Y}}_{\text{sps}}$  for initialization.
2: for  $i = 1$  to  $I_{\text{max}}$  do
3:   for  $n = 1$  to 6 do
4:     Construct mode- $n$  matricization  $\hat{\mathbf{Y}}_{\text{sps},(n)}$  of  $\hat{\mathcal{Y}}_{\text{sps}}$ .
5:     Update factor estimate  $\hat{\mathbf{B}}_n$  using (51).
6:   end for
7:   Obtain tensor estimate  $\hat{\mathcal{Y}}_{\text{sps}}^i = \llbracket \mathbf{1}_R; \hat{\mathbf{B}}_1, \hat{\mathbf{B}}_2, \dots, \hat{\mathbf{B}}_6 \rrbracket$ .
8:   if  $\|\hat{\mathcal{Y}}_{\text{sps}}^i - \hat{\mathcal{Y}}_{\text{sps}}^{i-1}\|_F / \|\hat{\mathcal{Y}}_{\text{sps}}^i\|_F < \epsilon$  then
9:     break.
10:  end if
11: end for
12: Perform Algorithms 2 and 3.
Output: Refined Channel-parameter estimates.

```

**Output:** Refined Channel-parameter estimates.

precise CP factors. In particular, factor estimators can be constructed by solving the following problem

$$\min_{\{\hat{\mathbf{B}}_n\}_{n=1}^6} \|\mathcal{Y}_{\text{sps}} - \llbracket \mathbf{1}_R; \hat{\mathbf{B}}_1, \hat{\mathbf{B}}_2, \hat{\mathbf{B}}_3, \hat{\mathbf{B}}_4, \hat{\mathbf{B}}_5, \hat{\mathbf{B}}_6 \rrbracket\|_F^2, \quad (50)$$

where weight  $\hat{\beta}$  is absorbed into any factor, e.g.,  $\hat{\mathbf{B}}_6 \leftarrow \hat{\mathbf{B}}_6 \text{diag}(\hat{\beta})$ . The ALS scheme alternately updates factor  $\hat{\mathbf{B}}_n$  by fixing the other factors and computing the least squares (LS) estimate as

$$\hat{\mathbf{B}}_n = \mathbf{Y}_{\text{sps},(n)} (\hat{\mathbf{B}}_6 \odot \dots \odot \hat{\mathbf{B}}_{n+1} \odot \hat{\mathbf{B}}_{n-1} \odot \dots \odot \hat{\mathbf{B}}_1)^* \mathbf{F}^*, \quad (51)$$

$$\mathbf{F} = (\hat{\mathbf{B}}_1^H \hat{\mathbf{B}}_1 \odot \dots \odot \hat{\mathbf{B}}_{n-1}^H \hat{\mathbf{B}}_{n-1} \odot \hat{\mathbf{B}}_{n+1}^H \hat{\mathbf{B}}_{n+1} \odot \dots \odot \hat{\mathbf{B}}_6^H \hat{\mathbf{B}}_6)^\dagger,$$

where  $\mathbf{Y}_{\text{sps},(n)}$  is the mode- $n$  matricization of  $\mathcal{Y}_{\text{sps}}$  formed by arranging the mode- $n$  fibers to be the columns of the resulting matrix [36].

The factor estimates  $\{\hat{\mathbf{B}}_n\}_{n=1}^6$  obtained in Stage II can be applied to initialize ALS. Once ALS converges under the preset threshold, new CP factors are acquired. Algorithms 2 and 3 can then be repeated to refine the channel-parameter estimates further. To update the delay estimates, column-wise element-space ESPRIT needs to be performed using the new  $\hat{\mathbf{B}}_1$  and/or  $\hat{\mathbf{B}}_6$ , similar to the implementation of transformed-space ESPRIT in (42). If both modes 1 and 6 are selected, the corresponding delay estimates are averaged and the mean value is output, as there is no clear indication of which is more accurate. It is observed that element-space ESPRIT alone suffices to ensure the accuracy of delay estimates, making the subsequent CBS refinement unnecessary. CE Stage III is outlined in Algorithm 4.

## IV. PERFORMANCE ANALYSIS

*A. CRLB Analysis*

In this subsection, the CRLB is determined to indicate the achievable optimal estimation precision. The CRLB is calculated from the inverse of the Fisher information matrix (FIM). In this paper, FIM is constructed from the real-valued

observation model by transforming the original complex-valued observation model into a real-valued one, i.e., partitioning the real and imaginary parts of the complex numbers. Before discussing the specific case, the FIM for the general real Gaussian scenario is first considered.

*Theorem 2:* Assume that  $\mathbf{x} \sim \mathcal{N}(\boldsymbol{\mu}(\phi), \mathbf{C}(\phi))$ , and hence both the mean  $\boldsymbol{\mu}(\phi)$  and covariance  $\mathbf{C}(\phi)$  may depend on parameter  $\phi$ . Let  $[\phi]_i = \phi_i$ , then the FIM is given by

$$[\mathbf{J}(\phi)]_{i,j} = \left[ \frac{\partial \boldsymbol{\mu}(\phi)}{\partial \phi_i} \right]^T \mathbf{C}^{-1}(\phi) \left[ \frac{\partial \boldsymbol{\mu}(\phi)}{\partial \phi_j} \right] + \frac{1}{2} \text{tr} \left[ \mathbf{C}^{-1}(\phi) \frac{\partial \mathbf{C}(\phi)}{\partial \phi_i} \mathbf{C}^{-1}(\phi) \frac{\partial \mathbf{C}(\phi)}{\partial \phi_j} \right]. \quad (52)$$

*Proof:* Details can be found in [42, Appendix 3C]. ■

For the case at hand, the real observation model can be expressed as

$$\hat{\mathbf{y}}^{(k,g)} = \tilde{\mathbf{y}}^{(k,g)}(\phi) + \tilde{\mathbf{w}}^{(k,g)}, \quad k = 1, \dots, K, g = 1, \dots, G, \quad (53)$$

where  $\tilde{\mathbf{y}}^{(k,g)} = [\Re(\mathbf{y}^{(k,g)})^T, \Im(\mathbf{y}^{(k,g)})^T]^T \in \mathbb{C}^{2N_1 N_2 \times 1}$  with  $\mathbf{y}^{(k,g)} = \mathbf{y}_L^{(k,g)} + \mathbf{y}_R^{(k,g)}$  being noise-free ensemble signal in (10),  $\tilde{\mathbf{w}}^{(k,g)} = [\Re(\mathbf{w}^{(k,g)})^T, \Im(\mathbf{w}^{(k,g)})^T]^T$ , and parameter  $\phi$  will be defined later.

Following [29, Appendix A], the covariance matrix of  $\tilde{\mathbf{w}}^{(k,g)}$  is  $\mathbf{C}^{(k,g)} = \mathbf{C}_B^{(k,g)} + \mathbf{C}_R^{(k,g)}$  with

$$\mathbf{C}_X^{(k,g)} = \frac{\sigma_X^2}{2} \begin{bmatrix} \Re(\mathbf{G}_X \mathbf{G}_X^H) \Im(\mathbf{G}_X \mathbf{G}_X^H)^T \\ \Im(\mathbf{G}_X \mathbf{G}_X^H) \Re(\mathbf{G}_X \mathbf{G}_X^H) \end{bmatrix}, \quad (54)$$

where  $X \in \{B, R\}$ ,  $\mathbf{G}_B = \mathbf{R}^H$ , and  $\mathbf{G}_R = \mathbf{R}^H \mathbf{H}_{R,2}^{(k)} \Gamma^{(g)}$ . We see that in our active-RIS scenario here, the covariance matrix  $\mathbf{C}^{(k,g)}$  is a function of  $\mathbf{H}_{R,2}^{(k)}$  and thus relevant to channel parameters. However, in the passive-RIS case without thermal noise at RIS (e.g., see [14], [21], [43]), the noise covariance (i.e.,  $\mathbf{C}^{(k,g)} = \mathbf{C}_B^{(k,g)}$ ) does not depend on channel parameters, hence the second term in (52) is zero, which is a special case of ours. Note that the active-RIS work in [29] has neglected the second term in (52).

Using (4),  $\mathbf{G}_R \mathbf{G}_R^H$  can be further expressed as

$$\mathbf{G}_R \mathbf{G}_R^H = \eta^2 M_y M_z \sum_q |\beta_{R,2}^{(q)}|^2 \mathbf{R}^H \mathbf{A}_B(\boldsymbol{\theta}_R^{(q)}) \mathbf{R} + \eta^2 \sum_{q \neq q'} \beta_{R,2}^{(q)} (\beta_{R,2}^{(q')})^* e^{j2\pi f^{(k)} (\tau_{R,2}^{(q')} - \tau_{R,2}^{(q)})} \mathbf{R}^H \bar{\mathbf{A}}_B \mathbf{R}, \quad (55)$$

where we have leveraged  $\Gamma^{(g)} (\Gamma^{(g)})^H = \eta^2 \mathbf{I}_{M_y M_z}$  as well as  $\mathbf{a}_R^T(\boldsymbol{\varphi}_D^{(q)}) \mathbf{a}_R^*(\boldsymbol{\varphi}_D^{(q)}) = M_y M_z$ , and

$$\mathbf{A}_B(\boldsymbol{\theta}_R^{(q)}) = \mathbf{a}_B(\boldsymbol{\theta}_R^{(q)}) \mathbf{a}_B^H(\boldsymbol{\theta}_R^{(q)}) \in \mathbb{C}^{\tilde{N}_y \tilde{N}_z \times \tilde{N}_y \tilde{N}_z}, \quad \bar{\mathbf{A}}_B = (\mathbf{a}_R^T(\boldsymbol{\varphi}_D^{(q)}) \mathbf{a}_R^*(\boldsymbol{\varphi}_D^{(q')})) \mathbf{a}_B(\boldsymbol{\theta}_R^{(q)}) \mathbf{a}_B^H(\boldsymbol{\theta}_R^{(q')}). \quad (56)$$

Note in (55) that the first term is greatly larger than the second term, owing to aligned phases in the first term. Therefore, it is reasonable to neglect the second term in (55) hereafter.

We determine the unknowns for CRLB calculation as follows. Firstly, the multipath parameters of interest (aiming to recover direct and cascaded channels) were listed at the end of Section II-B. Define  $\boldsymbol{\tau}_L \in \mathbb{R}^{L \times 1}$ ,  $\boldsymbol{\tau}_R \in \mathbb{R}^{C \times 1}$ ,  $\boldsymbol{\psi}_{2(3)} \in \mathbb{R}^{C \times 1}$ ,  $\boldsymbol{\theta}_L \in \mathbb{R}^{2L \times 1}$ ,  $\boldsymbol{\theta}_R \in \mathbb{R}^{2Q \times 1}$ ,  $\boldsymbol{\beta}_L \in \mathbb{R}^{L \times 1}$ , and  $\boldsymbol{\beta}_R \in \mathbb{R}^{C \times 1}$  as

the vector collection of  $\{\boldsymbol{\tau}_L^{(\ell)}\}$ ,  $\{\boldsymbol{\tau}_R^{(p,q)}\}$ ,  $\{\boldsymbol{\psi}_{2(3)}^{(p,q)}\}$ ,  $\{\boldsymbol{\theta}_{L,az}^{(\ell)}, \boldsymbol{\theta}_{L,el}^{(\ell)}\}$ ,  $\{\boldsymbol{\theta}_{R,az}^{(q)}, \boldsymbol{\theta}_{R,el}^{(q)}\}$ ,  $\{\boldsymbol{\beta}_L^{(\ell)}\}$ , and  $\{\boldsymbol{\beta}_R^{(p,q)}\}$ , respectively. Let  $\boldsymbol{\beta}_{L(R),\Re} = \Re(\boldsymbol{\beta}_{L(R)})$  and  $\boldsymbol{\beta}_{L(R),\Im} = \Im(\boldsymbol{\beta}_{L(R)})$ . Then we can form parameter vector of interest of dimension  $5R + 2Q$  as

$$\boldsymbol{\phi}_{\text{int}} = [\boldsymbol{\tau}_L^T, \boldsymbol{\tau}_R^T, \boldsymbol{\psi}_2^T, \boldsymbol{\psi}_3^T, \boldsymbol{\theta}_L^T, \boldsymbol{\theta}_R^T, \boldsymbol{\beta}_{L,\Re}^T, \boldsymbol{\beta}_{L,\Im}^T, \boldsymbol{\beta}_{R,\Re}^T, \boldsymbol{\beta}_{R,\Im}^T]^T.$$

Secondly, the nuisance parameters generated from the covariance term in (55) construct the vector  $\boldsymbol{\phi}_{\text{nu}} = [|\beta_{R,2}^{(1)}|^2, \dots, |\beta_{R,2}^{(Q)}|^2]^T \in \mathbb{R}^{Q \times 1}$ . Consequently, the overall parameter vector becomes  $\boldsymbol{\phi} = [\boldsymbol{\phi}_{\text{int}}^T, \boldsymbol{\phi}_{\text{nu}}^T]^T \in \mathbb{R}^{(5R+3Q) \times 1}$ .

With (53), we have  $\hat{\mathbf{y}}^{(k,g)} \sim \mathcal{N}(\tilde{\mathbf{y}}^{(k,g)}(\phi), \mathbf{C}^{(k,g)}(\phi))$ . Based on Theorem 2, we can compute the FIM  $\mathbf{J}^{(k,g)}(\phi)$  for each  $k \in \{1, \dots, K\}$  and each  $g \in \{1, \dots, G\}$ . The trivial derivatives in FIM calculation are concluded in Appendix A. Thus, the ensemble FIM across all subcarriers and slots is expressed as

$$\mathbf{J}(\phi) = \sum_{k=1}^K \sum_{g=1}^G \mathbf{J}^{(k,g)}(\phi) \in \mathbb{R}^{(5R+3Q) \times (5R+3Q)}. \quad (57)$$

Our interest is to determine the performance bound for  $\boldsymbol{\phi}_{\text{int}}$ . Therefore, invoke the inverse formula of a partitioned matrix [44] for the  $(5R + 2Q) \times (5R + 2Q)$  upper left block, yielding the equivalent FIM for  $\boldsymbol{\phi}_{\text{int}}$  only as

$$\check{\mathbf{J}}(\boldsymbol{\phi}_{\text{int}}) = \mathbf{J}_1 - \mathbf{J}_2 \mathbf{J}_3^{-1} \mathbf{J}_2^T, \quad \mathbf{J}(\phi) = \begin{bmatrix} \mathbf{J}_1 & \mathbf{J}_2 \\ \mathbf{J}_2^T & \mathbf{J}_3 \end{bmatrix}. \quad (58)$$

The CRLBs for elements in  $\boldsymbol{\phi}_{\text{int}}$  hold

$$\text{CRLB}([\boldsymbol{\phi}_{\text{int}}]_s) = [\check{\mathbf{J}}^{-1}(\boldsymbol{\phi}_{\text{int}})]_{s,s}, \quad s = 1, \dots, 5R + 2Q. \quad (59)$$

## B. Complexity Analysis

The complexity of the proposed algorithms and the benchmarking methods is analyzed next. To simplify the analysis, it is set that  $K_1 = K_2$ ,  $G_1 = G_2$ , and  $N_1 = N_2$ ; thus, their subscripts 1 and 2 are omitted in this subsection. The CPDs in baseline methods are realized via ALS, and all ALS mechanisms require  $T$  iterations.

Our main CE framework can be divided into four parts: VSCPD and CE Stages I–III. Let us start with the complexity of VSCPD. The compact SVD of  $\mathbf{Y}_{\text{sps},[3]}$  involves a complexity of  $\mathcal{O}(K^3 G^2 N^4)$ . Recovering delays using element-space ESPRIT introduces a complexity of  $\mathcal{O}(R^2 K G^2)$ . The complexity of constructing  $\{\hat{\mathbf{b}}_{n,r}\}_{r=1}^R$ ,  $n = 2, 3, 4, 5$  via SVD is in the order of  $\mathcal{O}(R(G^3 + N^3))$ . In CE Stage I, the column-wise transformed-space ESPRIT takes the complexity of  $\mathcal{O}(CG + RN)$ . In Stage II, we assume that  $E_n = E_{n'}$  and  $I_n = I_{n'}$  for distinct  $n$  and  $n'$ , thus we ignore their subscript  $n$ . The CBS involves a complexity of  $\mathcal{O}(IE(CG + RN))$ . In Stage III, the complexity of ALS is in the order of  $\mathcal{O}(TRKGN(KGN + RGN + RKN + RKG))$ . In a nutshell, our complexities at the end of CE Stages I–III are

$$\begin{aligned} \mathcal{O}_I &= \mathcal{O}(K^3 G^2 N^4) + \mathcal{O}(R^2 K G^2) + \mathcal{O}(RG^3) + \mathcal{O}(RN^3), \\ \mathcal{O}_{II} &= \mathcal{O}_I + \mathcal{O}(IECG) + \mathcal{O}(IERN), \\ \mathcal{O}_{III} &= \mathcal{O}(K^3 G^2 N^4) + \mathcal{O}(TRK^2 G^2 N^2) + \mathcal{O}(TR^2 K G^2 N^2) \\ &\quad + \mathcal{O}(TR^2 K^2 G N^2) + \mathcal{O}(TR^2 K^2 G^2 N) + \mathcal{O}(RG^3) \\ &\quad + \mathcal{O}(RN^3) + \mathcal{O}(IECG) + \mathcal{O}(IERN). \end{aligned} \quad (60)$$

The work in [41] introduced a pioneering tensor-based CE method. This approach initially applies ALS-CPD to extract the factors, followed by an exhaustive grid-based CBS to recover the channel parameters. The ALS-CPD's complexity is in the same order as described before (60). Additionally, assuming that  $S$  searches are required for each exhaustive CBS, the total complexity of the CBS process is  $\mathcal{O}(S(RK + CG + RN))$ . In conclusion, the overall complexity comes to

$$\begin{aligned} & \mathcal{O}(TRK^2G^2N^2) + \mathcal{O}(TR^2KG^2N^2) + \mathcal{O}(TR^2K^2GN^2) \\ & + \mathcal{O}(TR^2K^2G^2N) + \mathcal{O}(SRK) + \mathcal{O}(SCG) + \mathcal{O}(SRN). \end{aligned}$$

Note that the iteration number of ALS-CPD required here is larger than ours in Stage III, as our Stage II has generated an accurate initialization for the subsequent iterative ALS. Furthermore, to attain comparable search performance, CBS here also requires much more searches than ours in Stage II, i.e.,  $S > IE$ , since we employ a modified iterative strategy and input coarse results obtained from Stage I.

Study [29] proposed a serial tensor-based CE approach tailored for the fully-LOS scenario ( $L = C = 1, R = 2$ ), a particular case of our multipath consideration. This mechanism sequentially involves CPD+ESPRIT two times and optional LS refinement. The complexities of CPDs are in the order of  $\mathcal{O}(TRN(KN + RN + RK))$  and  $\mathcal{O}(TCG(G + C))$ . The ESPRIT estimations introduce complexities of  $\mathcal{O}(R(K + N))$  and  $\mathcal{O}(CG)$ . However, the complexity of the LS step can not be evaluated well in theory since this issue is smartly addressed by the MATLAB toolbox without a specific solution. The complexity at the end of the ESPRIT step (without LS refinement) becomes

$$\mathcal{O}(TRKN^2) + \mathcal{O}(TR^2N^2) + \mathcal{O}(TR^2KN) + \mathcal{O}(TG^2). \quad (61)$$

## V. NUMERICAL RESULTS

This section evaluates the CE performance of our algorithms via simulation experiments. The derived CRLB in Section IV-A is applied as an estimation accuracy metric. Furthermore, benchmarking accuracy is provided from existing methods: CPD+ESPRIT+LS [29] (optional LS refinement), CPD+CBS [41], and VSCPD+CBS [25]. Notably, the last two baseline schemes above originally did not aim to solve the current CE issue in this paper. Unlike our modified iterative search strategy in CE Stage II, they have simply invoked exhaustive grid-based CBS. Their exhaustive search scheme is retained, but to apply to the current CE scenario, CPD is extended to decompose expanded tensor  $\hat{\mathbf{Y}}_{\text{sps}}$  in CPD+CBS and directly employs our VSCPD in VSCPD+CBS. All experiments are conducted in a PC using MATLAB R2022b with Intel(R) Core(TM) i9-14900HX 2.20 GHz CPU and 16GB RAM.

### A. Simulation Settings and Performance Metrics

The array size of RIS is  $M_y = M_z = 15$ . As for the size of BS, we set  $\tilde{N}_y = \tilde{N}_z = 10$  and  $N_1 = N_2 = 5$ . The bandwidth is 320 MHz with central carrier frequency  $f_c = 28$  GHz. There are  $K_0 = 128$  subcarriers, of which the first  $K = 32$  subcarriers are pilots. The number of time slots is  $G = 49$ . The transmit power is set to  $\mathbf{P}_T = 7$  dBm, and

the power of active RIS is restricted to  $\mathbf{P}_R = 1.76$  dBm. The noise power spectral densities (PSDs) at both BS and RIS are  $-174$  dBm/Hz, and their noise figures are identically 10 dB. The element spacings of BS and RIS are  $d_B = 0.5\lambda$  and  $d_R = 0.1\lambda$ , respectively, and wavelength  $\lambda = \frac{c}{f_c}$  with light speed  $c$ . The multipath numbers are  $L = P = Q = 2$ , and thus  $R = 6$ . Delays, AOAs, AODs, and path gains are generated according to practical geometric models specified in [29], and the same LOS settings are employed as shown in [29, Table I]. Additionally, the scatterers for UE-BS, UE-RIS, and RIS-BS links are located at  $[4, 4, 2]^T$  m,  $[-2, -4, 1]^T$  m, and  $[-1, 1, 5]^T$  m, respectively. The delays are expressed in meter units by multiplying light speed, and the angles are in degree units. The received signal-to-noise ratio (SNR) is defined as

$$\text{SNR} = \frac{\sum_{k=1}^K \sum_{g=1}^G \|\mathbf{y}^{(k,g)}\|^2}{\sum_{k=1}^K \sum_{g=1}^G \text{tr}(\mathbf{C}^{(k,g)})}. \quad (62)$$

Tensor operations are programmed based on the Tensorlab toolbox [45]. The spatial smoothing parameter is set to  $K_1 = 15$  with  $K_1 + K_2 - 1 = K$ . Always, set  $G_1 = G_2$  with  $G = G_1G_2$ . The generators of Vandermonde matrices  $\{\mathbf{T}_n\}_{n=2}^5$  are randomly drawn. In our CE Stage II,  $E_n = 2\tilde{E} + 1$  with  $\tilde{E} = 100$ ,  $I_n = 8$ ,  $\zeta_n = 0.5$ , and  $\Delta_n^1 = \frac{U_n}{10C}$  with parameter range  $(-U_n, U_n)$ . To appraise the search accuracy using identical search numbers, we use 1608 searches in the CBS part of the VSCPD+CBS scheme. Moreover, the search number in CBS of CPD+CBS approach is set as  $10^4$ , much greater than ours. In the proposed CE Stage III, the convergence tolerance for ALS is set to  $10^{-8}$ . The convergence tolerance for ALS-CPD in benchmarking methods is designed as  $10^{-15}$ , which is significantly smaller than ours, as the ALS-CPD performance becomes undesirable using a larger tolerance in multipath scenarios. The LS refinement in the CPD+ESPRIT+LS approach is realized by Manopt toolbox [46] with 40 times the maximum iterations. The preceding settings are applied to the following simulations unless otherwise specified.

Root mean squared error (RMSE) is used to evaluate the accuracy of channel-parameter estimators. That is,

$$\text{RMSE}(\boldsymbol{\xi}) = \sqrt{\mathbb{E}[\|\hat{\boldsymbol{\xi}} - \boldsymbol{\xi}\|^2]}, \quad (63)$$

where  $\boldsymbol{\xi}$  can be any multipath-parameter vector/scalar, and  $\hat{\boldsymbol{\xi}}$  denotes its estimate. Due to the permutation ambiguity in the parameter estimates, every RMSE is determined after sorting both the ground truth and estimated values. Furthermore, the estimation accuracy of the signal tensor is leveraged as a comprehensive performance metric for all channel-parameter estimates. The recovery precision of the signal tensor is evaluated using normalized MSE (NMSE), defined as

$$\text{NMSE}(\mathcal{Y}) = \frac{\mathbb{E}[\|\mathcal{Y}(\hat{\phi}_{\text{int}}) - \mathcal{Y}(\phi_{\text{int}})\|_F^2]}{\|\mathcal{Y}(\phi_{\text{int}})\|_F^2}, \quad (64)$$

where  $\hat{\phi}_{\text{int}}$  is the estimated version of  $\phi_{\text{int}}$ . The statistical expectation is approximately computed via the average result over  $10^3$  Monte Carlo trials.

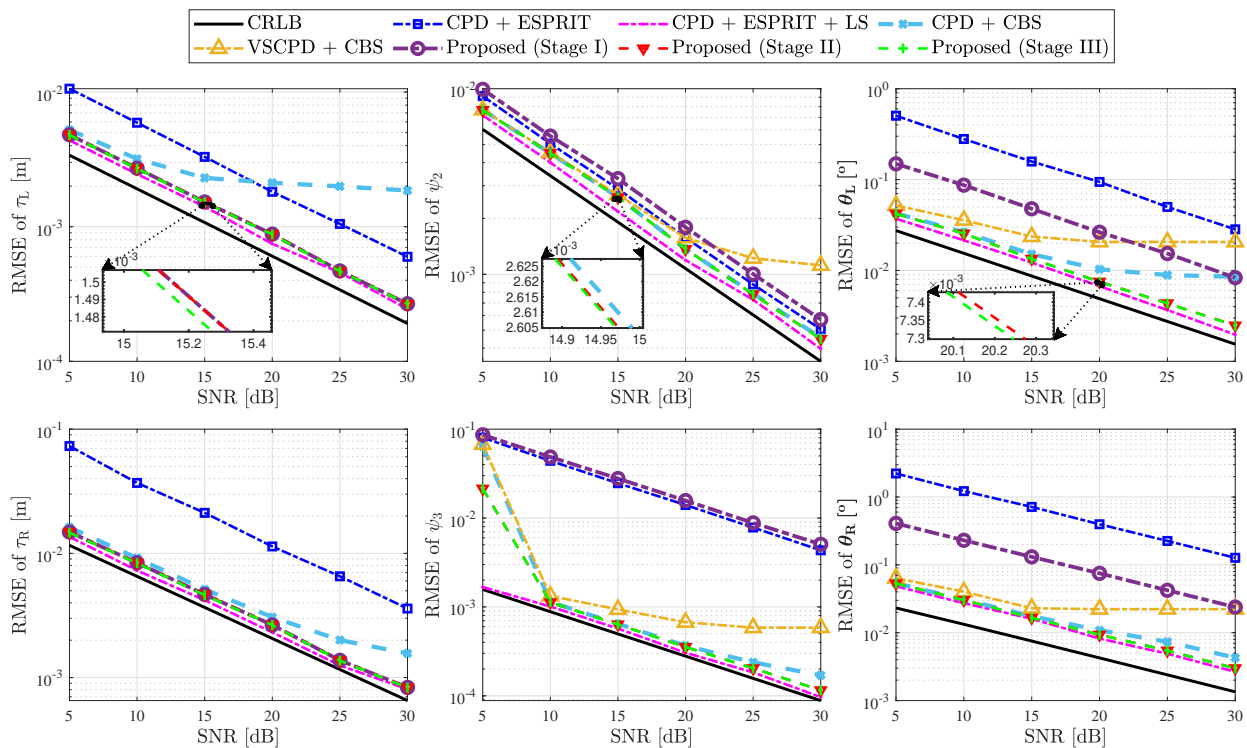


Fig. 3. RMSEs of  $\tau_L$ ,  $\tau_R$ ,  $\psi_2$ ,  $\psi_3$ ,  $\theta_L$ , and  $\theta_R$  versus SNR in LOS scenario.

### B. CE in LOS Scenario

Recall that the competing algorithm CPD+ESPRIT+LS is tailored for the LOS scenario, and its performance undoubtedly degrades in the multipath scenario. The estimation performance in the LOS case is first discussed for a fair comparison. For this, remove all scatterers and let  $L = P = Q = 1$  with  $R = 2$ . To reserve the parameter designs in the original CPD+ESPRIT+LS implementation, parameters are set as  $G = 9$  and  $P_R = 7$  dBm. In our Stage III, the convergence tolerance for ALS is shrunk to  $10^{-12}$  for better performance.

1) *Estimation Accuracy*: We range the SNR from 5 dB to 30 dB in 5 dB increments. The estimation performance of channel parameters is depicted in Fig. 3. The delay RMSEs from the VSCP+CBS method are omitted, as the delay estimation is performed similarly. Algebraic ESPRIT-based methods generally show inferior performance, with significant gaps compared to the corresponding CRLBs. Fortunately, Stage I significantly outperforms CPD+ESPRIT in delay and AOA accuracy thanks to our superior spatial smoothing and VSCP techniques, which enhance tensor factorization performance across most modes compared to the ALS-CPD scheme.

CBS-based (or ML-like) methods basically further improve accuracy over ESPRIT methods. Stage II demonstrates notable performance gains in high-SNR scenarios compared to CPD+CBS (which involves more extensive searches) and VSCP+CBS (with the same number of searches), highlighting the effectiveness of the modified search strategy, where search space is iteratively constructed with coarse initialization from Stage I. Both Stage III and the existing LS technique can further refine previous estimates, with LS refinement offering better performance at the cost of greatly increased complexity

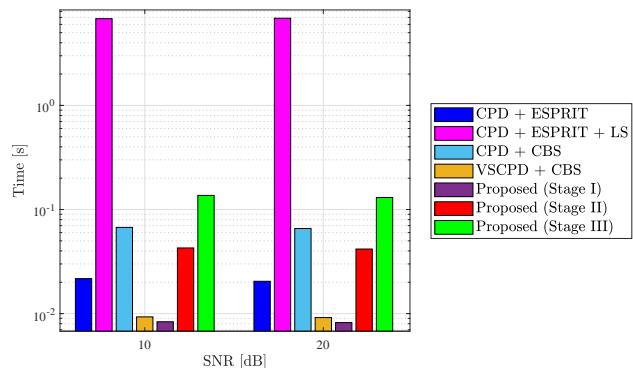


Fig. 4. Average computation time with varying SNR in LOS scenario.

(to be shown soon). However, the high complexity of LS refinement is impractical in multipath scenarios, where the number of optimization variables increases significantly.

2) *Implementation Complexity*: The average CPU run time of different algorithms is presented in Fig. 4, with SNR  $\in \{10, 20\}$  dB. The computation time decreases marginally for each algorithm with ascending SNR. For algorithm comparison, specific run time is listed hereafter for 10 dB SNR. The complexity of our CE framework increases as the stage-wise process develops. Our Stage I enjoys the lowest complexity (8.35 ms), only 38.5% of CPD+ESPRIT (21.67 ms). This is owing to the algebraic implementation of our VSCP in contrast to the iterative ALS-CPD. Furthermore, the complexity of our Stage II with a modified search strategy is lower than CPD+CBS and greater than VSCP+CBS. As mentioned,

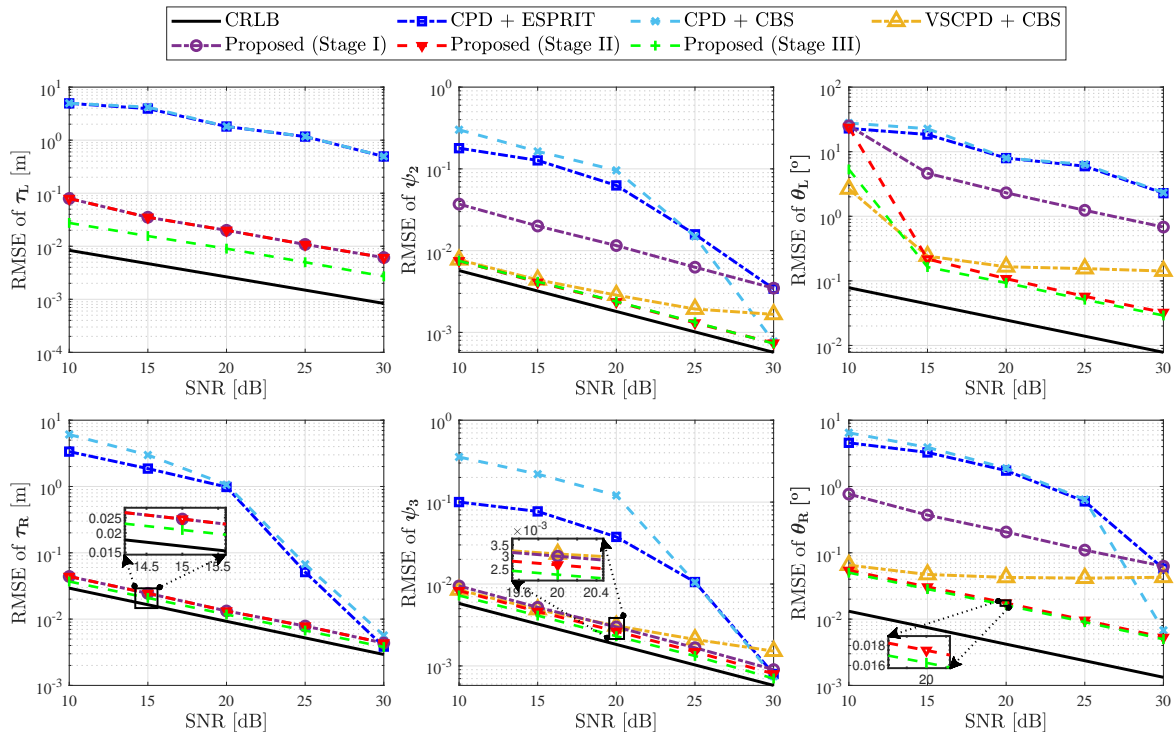


Fig. 5. RMSEs of  $\tau_L$ ,  $\tau_R$ ,  $\psi_2$ ,  $\psi_3$ ,  $\theta_L$ , and  $\theta_R$  versus SNR in multipath scenario.

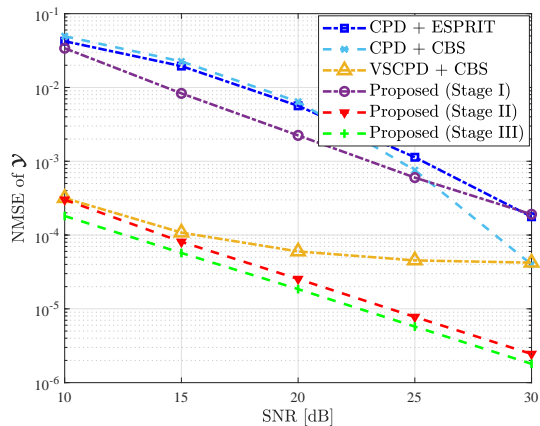


Fig. 6. NMSE of  $\mathcal{Y}$  versus SNR in multipath scenario.

proposed Stage II has an accuracy advantage over these two existing CBS-based methods, especially in high-SNR cases. Significantly, the complexity of our Stage III (0.14 s) is only 2.1% of LS-refined algorithm (6.81 s), tremendously saving the computation time with a theoretical specific solution.

### C. CE in Multipath Scenarios

The CPD+ESPRIT method, initially designed for LOS scenarios, is extended to the multipath case; however, the subsequent LS refinement is no longer feasible due to its significant computational complexity. Additionally, algorithms may fail based on the criteria outlined in Section III-D, specifically the *variance principle* and *similarity principle*.

Each RMSE/NMSE result is reported from  $10^3$  successful runs out of a minimum of  $10^3$  total trials. In this context, the success rate is an additional evaluation metric for tensor decomposition performance, defined as the ratio of successful runs to the total number of trials.

1) *Estimation Accuracy in Varying-SNR Scenario*: In this scenario, the SNR varies from 10 dB to 30 dB in 5 dB increments. The RMSEs of channel parameters and the NMSE of the signal tensor are presented in Fig. 5 and Fig. 6, respectively. Delay results using VSCPD+CBS are omitted in Fig. 5. The estimation performance of our CE framework improves sequentially through two stages of refinement, consistent with the results in Fig. 3. The CPD+ESPRIT and CPD+CBS schemes exhibit similar but poor accuracy, both inferior to Stage I in general. This indicates that classical CPD is unsuitable for scenarios with rank-deficient factor matrices, and our VSCPD effectively addresses this issue by leveraging the Vandermonde structure. Furthermore, Stage II outperforms VSCPD+CBS in accuracy under high-SNR conditions, benefiting from a superior iterative search scheme. Table I presents the success rates of the existing ALS-CPD and the proposed VSCPD in the varying-SNR scenario. While the probability of success for ALS-CPD increases with higher SNR, VSCPD consistently achieves perfect success, indicating its superiority.

2) *Estimation Accuracy in Varying-K Scenario*: In this scenario, the training subcarrier number  $K$  is adjusted from 16 to 48 in increments of 8, with  $K_1$  consistently set to  $0.5K$ . The SNR remains fixed at 15 dB. Fig. 7 illustrates the NMSE results for this varying- $K$  scenario. As  $K$  increases, the NMSEs of the two ALS-CPD-based approaches initially rise and then fall, with the worst performance observed at

TABLE I  
SUCCESS RATES OF TENSOR DECOMPOSITION VERSUS SNR

	10 dB	15 dB	20 dB	25 dB	30 dB
ALS-CPD	80.2%	90.4%	97.4%	99.2%	99.8%
VSCPD	100%	100%	100%	100%	100%

TABLE II  
SUCCESS RATES OF TENSOR DECOMPOSITION VERSUS  $K$

	$K = 16$	$K = 24$	$K = 32$	$K = 40$	$K = 48$
ALS-CPD	94.0%	93.6%	90.1%	90.3%	90.8%
VSCPD	100%	100%	100%	100%	100%

$K = 32$ . Increasing  $K$  provides more training subcarriers, benefiting estimator performance; but it also increases the tensor dimension, making CPD more challenging. Fortunately, our algorithms avoid the curse of dimensionality, resulting in decreasing NMSEs as  $K$  grows. The successive refinements within our CE framework are also evident in Fig. 7. The success rates for the varying- $K$  scenario are summarized in Table II. The success rate of ALS-CPD exhibits an opposite trend to its NMSEs (Fig. 7), while the proposed VSCPD consistently achieves perfect results, demonstrating significant stability.

3) *Implementation Complexity*: The CPU run time for the multipath scenario is presented in Fig. 8. For the analysis, the parameter  $K \in \{16, 32, 48\}$  with  $K_1 = 0.5K$  and  $N_1 = N_2 \in \{4, 5, 6\}$ . The SNR is fixed at 15 dB. The results indicate that the complexity of each method increases with the rise in  $K$  and  $N_1$ . Run time is provided for the case  $K = 32, N_1 = 5$  for a more detailed algorithm comparison. The Stage I algorithm exhibits the lowest complexity at 22.26 ms, slightly lower than that of the VSCPD+CBS method, which takes 25.97 ms. Stage II has an intermediate complexity of 88.97 ms. Notably, Stage III shows a complexity of 0.63 s, comparable to those of two ALS-CPD approaches, highlighting the time-intensive nature of ALS-CPD for the multipath case.

## VI. CONCLUSION

This paper addressed the CE challenge for active RIS-assisted SIMO-OFDM wireless systems in multipath environments. Channels were modeled with multipath parameters, including path gains, delays, AOA, and AODs, transforming the CE problem into a parameter recovery task. A fifth-order CP tensor was constructed from the received signal using customized designs. Involving five factor matrices, four of which suffered from rank deficiency, while the other exhibited a Vandermonde structure. Spatial smoothing was applied to extend the original tensor, and an efficient VSCPD method was developed to extract the factor matrices. A triple-stage CE framework, consisting of coarse estimation in Stage I and successive optional refinements in Stages II and III, was proposed. The CRLB was derived with the noise covariance matrix dependent on multipath parameters, and the implementation complexity of the proposed and benchmark algorithms was analyzed. Simulation results demonstrated the superiority of the proposed methods across various evaluation metrics. Future research directions include extending CE to the

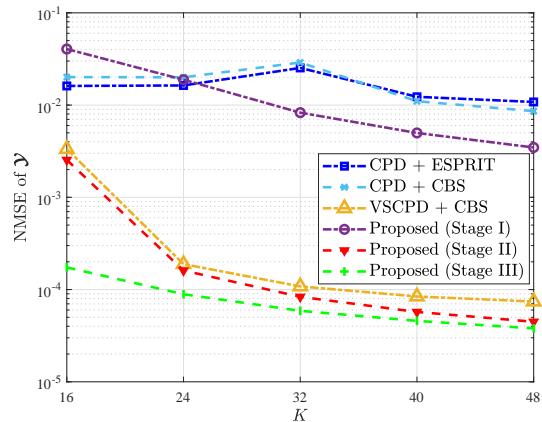


Fig. 7. NMSE of  $\mathcal{Y}$  versus  $K$  in multipath scenario.

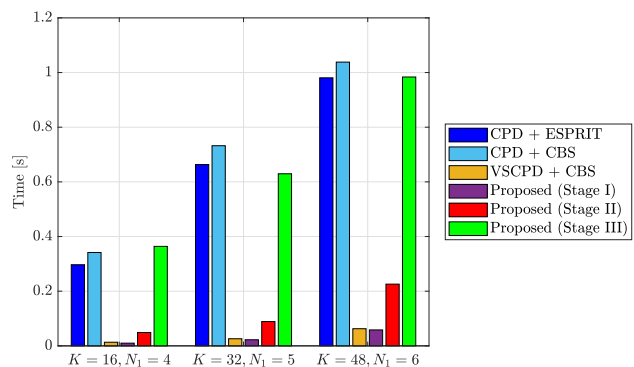


Fig. 8. Average computation time with varying  $K$  and  $N_1 = N_2$  in multipath scenario.

multiple-input multiple-output (MIMO) scenario, and the joint RIS calibration and user positioning problem using channel parameters.

## ACRONYMS

ALS	alternating least squares
AOA/AOD	angle-of-arrival/departure
BS	base station
CBS	correlation-based search
CE	channel estimation
CPD	canonical polyadic decomposition
CRLB	Cramér-Rao lower bound
CSI	channel state information
LOS	line-of-sight
LS	least squares
ML	maximum likelihood
mmWave	millimeter wave
OFDM	orthogonal frequency-division multiplexing
RIS	reconfigurable intelligent surface
SIMO	single-input multiple-output
UAV	unmanned aerial vehicle
UE	user equipment
VSCPD	Vandermonde structured CPD

APPENDIX A  
PARTIAL DERIVATIVES IN FIM CALCULATION

Firstly, we define

$$\begin{aligned}
\beta_{L,\mathfrak{R}}^{(\ell)} &= \mathfrak{R}(\beta_L^{(\ell)}), \quad \beta_{L,\mathfrak{J}}^{(\ell)} = \mathfrak{J}(\beta_L^{(\ell)}), \\
\beta_{R,\mathfrak{R}}^{(p,q)} &= \mathfrak{R}(\beta_R^{(p,q)}), \quad \beta_{R,\mathfrak{J}}^{(p,q)} = \mathfrak{J}(\beta_R^{(p,q)}), \\
\Omega^{(k)} &= 2\pi f^{(k)}, \\
\delta_L^{(k,\ell)} &= e^{-j\Omega^{(k)}\tau_L^{(\ell)}}, \quad \delta_R^{(k,p,q)} = e^{-j\Omega^{(k)}\tau_R^{(p,q)}}, \\
\dot{\delta}_L^{(k,\ell)} &= -j\Omega^{(k)}\delta_L^{(k,\ell)}, \quad \dot{\delta}_R^{(k,p,q)} = -j\Omega^{(k)}\delta_R^{(k,p,q)}, \\
\check{\mathbf{a}}_R^{(p,q)} &= \mathbf{a}_R(\varphi_A^{(p)}) \otimes \mathbf{a}_R(\varphi_D^{(q)}), \\
\dot{\mathbf{a}}_{R,2(3)}^{(p,q)} &= j\frac{2\pi}{\lambda}\check{\mathbf{a}}_R^{(p,q)} \otimes [\mathbf{P}_R]_{:,2(3)}, \\
\boldsymbol{\theta} &= [\theta_{az}, \theta_{el}]^T, \\
\dot{\mathbf{d}}_{az}(\boldsymbol{\theta}) &= [0, \cos(\theta_{az}) \cos(\theta_{el}), 0]^T, \\
\dot{\mathbf{d}}_{el}(\boldsymbol{\theta}) &= [0, -\sin(\theta_{az}) \sin(\theta_{el}), \cos(\theta_{el})]^T, \\
\dot{\mathbf{a}}_{B,az(el)}(\boldsymbol{\theta}) &= j\frac{2\pi}{\lambda}\mathbf{a}_B(\boldsymbol{\theta}) \otimes (\mathbf{P}_B \dot{\mathbf{d}}_{az(el)}(\boldsymbol{\theta})), \\
\mathbf{P}_{B,i,j} &= [\mathbf{P}_B]_{i,:}^T - [\mathbf{P}_B]_{j,:}^T, \\
[\dot{\mathbf{A}}_{B,az(el)}(\boldsymbol{\theta})]_{i,j} &= j\frac{2\pi}{\lambda}(\mathbf{P}_B^T)_{i,j} \dot{\mathbf{d}}_{az(el)}(\boldsymbol{\theta}) [\mathbf{A}_B(\boldsymbol{\theta})]_{i,j}, \quad i \neq j, \\
[\dot{\mathbf{A}}_{B,az(el)}(\boldsymbol{\theta})]_{i,j} &= 0, \quad i = j.
\end{aligned}$$

Note that for complex-valued function  $\mathbf{F}(\phi)$  with respect to real-valued scalar  $\phi$ , we have

$$\frac{\partial \mathfrak{R}(\mathbf{F}(\phi))}{\partial \phi} = \mathfrak{R}\left(\frac{\partial \mathbf{F}(\phi)}{\partial \phi}\right), \quad \frac{\partial \mathfrak{J}(\mathbf{F}(\phi))}{\partial \phi} = \mathfrak{J}\left(\frac{\partial \mathbf{F}(\phi)}{\partial \phi}\right).$$

Furthermore, notice that  $\mathbf{y}_L^{(k,g)}$  degrades into  $\mathbf{y}_L^{(k)}$  in our case due to the identical pilot design before (41).

In the following, we only list the non-zero partial derivatives. Other derivatives required by the FIM computation are all zeros.

### A.1 Derivatives in the First Term of (52)

$$\begin{aligned}
\frac{\partial \mathbf{y}_L^{(k)}}{\partial \tau_L^{(\ell)}} &= x\beta_L^{(\ell)}\dot{\delta}_L^{(k,\ell)}\mathbf{R}^H \mathbf{a}_B(\boldsymbol{\theta}_L^{(\ell)}), \\
\frac{\partial \mathbf{y}_R^{(k,g)}}{\partial \tau_R^{(p,q)}} &= x\beta_R^{(p,q)}\rho_R^{(p,q)}\dot{\delta}_R^{(k,p,q)}\mathbf{R}^H \mathbf{a}_B(\boldsymbol{\theta}_R^{(q)}), \\
\frac{\partial \mathbf{y}_R^{(k,g)}}{\partial \psi_2^{(p,q)}} &= x\beta_R^{(p,q)}\delta_R^{(k,p,q)}((\boldsymbol{\gamma}^{(g)})^T \dot{\check{\mathbf{a}}}_{R,2}^{(p,q)})\mathbf{R}^H \mathbf{a}_B(\boldsymbol{\theta}_R^{(q)}), \\
\frac{\partial \mathbf{y}_R^{(k,g)}}{\partial \psi_3^{(p,q)}} &= x\beta_R^{(p,q)}\delta_R^{(k,p,q)}((\boldsymbol{\gamma}^{(g)})^T \dot{\check{\mathbf{a}}}_{R,3}^{(p,q)})\mathbf{R}^H \mathbf{a}_B(\boldsymbol{\theta}_R^{(q)}), \\
\frac{\partial \mathbf{y}_L^{(k)}}{\partial \theta_{L,az}^{(\ell)}} &= x\beta_L^{(\ell)}\delta_L^{(k,\ell)}\mathbf{R}^H \dot{\mathbf{a}}_{B,az}(\boldsymbol{\theta}_L^{(\ell)}), \\
\frac{\partial \mathbf{y}_L^{(k)}}{\partial \theta_{L,el}^{(\ell)}} &= x\beta_L^{(\ell)}\delta_L^{(k,\ell)}\mathbf{R}^H \dot{\mathbf{a}}_{B,el}(\boldsymbol{\theta}_L^{(\ell)}), \\
\frac{\partial \mathbf{y}_R^{(k,g)}}{\partial \theta_{R,az}^{(q)}} &= \sum_{p=1}^P x\beta_R^{(p,q)}\rho_R^{(p,q)}\delta_R^{(k,p,q)}\mathbf{R}^H \dot{\mathbf{a}}_{B,az}(\boldsymbol{\theta}_R^{(q)}),
\end{aligned}$$

$$\begin{aligned}
\frac{\partial \mathbf{y}_R^{(k,g)}}{\partial \theta_{R,el}^{(q)}} &= \sum_{p=1}^P x\beta_R^{(p,q)}\rho_R^{(p,q)}\delta_R^{(k,p,q)}\mathbf{R}^H \dot{\mathbf{a}}_{B,el}(\boldsymbol{\theta}_R^{(q)}), \\
\frac{\partial \mathbf{y}_L^{(k)}}{\partial \beta_{L,\mathfrak{R}}^{(\ell)}} &= x\delta_L^{(k,\ell)}\mathbf{R}^H \mathbf{a}_B(\boldsymbol{\theta}_L^{(\ell)}), \\
\frac{\partial \mathbf{y}_L^{(k)}}{\partial \beta_{L,\mathfrak{J}}^{(\ell)}} &= jx\delta_L^{(k,\ell)}\mathbf{R}^H \mathbf{a}_B(\boldsymbol{\theta}_L^{(\ell)}), \\
\frac{\partial \mathbf{y}_R^{(k,g)}}{\partial \beta_{R,\mathfrak{R}}^{(p,q)}} &= x\rho_R^{(p,q)}\delta_R^{(k,p,q)}\mathbf{R}^H \mathbf{a}_B(\boldsymbol{\theta}_R^{(q)}), \\
\frac{\partial \mathbf{y}_R^{(k,g)}}{\partial \beta_{R,\mathfrak{J}}^{(p,q)}} &= jx\rho_R^{(p,q)}\delta_R^{(k,p,q)}\mathbf{R}^H \mathbf{a}_B(\boldsymbol{\theta}_R^{(q)}).
\end{aligned}$$

### A.2 Derivatives in the Second Term of (52)

$$\begin{aligned}
\frac{\partial \mathbf{G}_R \mathbf{G}_R^H}{\partial \theta_{R,az}^{(q)}} &= \eta^2 M_y M_z |\beta_{R,2}^{(q)}|^2 \mathbf{R}^H \dot{\mathbf{A}}_{B,az}(\boldsymbol{\theta}_R^{(q)}) \mathbf{R}, \\
\frac{\partial \mathbf{G}_R \mathbf{G}_R^H}{\partial \theta_{R,el}^{(q)}} &= \eta^2 M_y M_z |\beta_{R,2}^{(q)}|^2 \mathbf{R}^H \dot{\mathbf{A}}_{B,el}(\boldsymbol{\theta}_R^{(q)}) \mathbf{R}, \\
\frac{\partial \mathbf{G}_R \mathbf{G}_R^H}{\partial |\beta_{R,2}^{(q)}|^2} &= \eta^2 M_y M_z \mathbf{R}^H \mathbf{A}_B(\boldsymbol{\theta}_R^{(q)}) \mathbf{R}.
\end{aligned}$$

### REFERENCES

- [1] Q. Wu and R. Zhang, "Intelligent reflecting surface enhanced wireless network via joint active and passive beamforming," *IEEE Trans. Wireless Commun.*, vol. 18, no. 11, pp. 5394–5409, Nov. 2019.
- [2] R. Li, B. Guo, M. Tao, Y.-F. Liu, and W. Yu, "Joint design of hybrid beamforming and reflection coefficients in RIS-aided mmWave MIMO systems," *IEEE Trans. Commun.*, vol. 70, no. 4, pp. 2404–2416, Apr. 2022.
- [3] Q. Wu, S. Zhang, B. Zheng, C. You, and R. Zhang, "Intelligent reflecting surface-aided wireless communications: A tutorial," *IEEE Trans. Commun.*, vol. 69, no. 5, pp. 3313–3351, May 2021.
- [4] C. Huang, A. Zappone, G. C. Alexandropoulos, M. Debbah, and C. Yuen, "Reconfigurable intelligent surfaces for energy efficiency in wireless communication," *IEEE Trans. Wireless Commun.*, vol. 18, no. 8, pp. 4157–4170, Aug. 2019.
- [5] L. Liu, S. Zhang, and S. Cui, "Leveraging a variety of anchors in cellular network for ubiquitous sensing," 2024, arXiv: 2403.17652.
- [6] Y. Liu et al., "Reconfigurable intelligent surfaces: Principles and opportunities," *IEEE Commun. Surv. & Tut.*, vol. 23, no. 3, pp. 1546–1577, Aug. 2021.
- [7] R. Long, Y.-C. Liang, Y. Pei, and E. G. Larsson, "Active reconfigurable intelligent surface-aided wireless communications," *IEEE Trans. Wireless Commun.*, vol. 20, no. 8, pp. 4962–4975, Aug. 2021.
- [8] R. Schroeder, J. He, G. Brante, and M. Juntti, "Two-stage channel estimation for hybrid RIS assisted MIMO systems," *IEEE Trans. Commun.*, vol. 70, no. 7, pp. 4793–4806, Jul. 2022.
- [9] G. Stuber, J. Barry, S. McLaughlin, Y. Li, M. Ingram, and T. Pratt, "Broadband MIMO-OFDM wireless communications," *Proc. IEEE*, vol. 92, pp. 271–294, Feb. 2004.
- [10] I. Barhum, G. Leus, and M. Moonen, "Optimal training design for MIMO OFDM systems in mobile wireless channels," *IEEE Trans. Signal Process.*, vol. 51, pp. 1615–1624, Jun. 2003.
- [11] H. Chen, F. Ahmad, S. Vorobyov, and F. Porikli, "Tensor decompositions in wireless communications and MIMO radar," *IEEE J. Sel. Topics Signal Process.*, vol. 15, no. 3, pp. 438–453, Apr. 2021.
- [12] X. Gong, W. Chen, L. Sun, J. Chen, and B. Ai, "An ESPRIT-based supervised channel estimation method using tensor train decomposition for mmWave 3-D MIMO-OFDM systems," *IEEE Trans. Signal Process.*, vol. 71, pp. 555–570, 2023.
- [13] Z. Zhou et al., "Channel estimation for millimeter-wave multiuser MIMO systems via PARAFAC decomposition," *IEEE Trans. Wireless Commun.*, vol. 15, no. 11, pp. 7501–7516, 2016.

- [14] L. Wei et al., "Channel estimation for RIS-empowered multi-user MISO wireless communications," *IEEE Trans. Commun.*, vol. 69, no. 6, pp. 4144–4157, Jun. 2021.
- [15] G. T. de Araujo, A. L. F. de Almeida, and R. Boyer, "Channel estimation for intelligent reflecting surface assisted MIMO systems: A tensor modeling approach," *IEEE J. Sel. Topics Signal Process.*, vol. 15, no. 3, pp. 789–802, Apr. 2021.
- [16] J. Du, Y. Cheng, L. Jin, and F. Gao, "Time-varying phase noise estimation, channel estimation, and data detection in RIS-assisted MIMO systems via tensor analysis," *IEEE Trans. Signal Process.*, vol. 71, pp. 3426–3441, 2023.
- [17] X. Shi, J. Wang, and J. Song, "Triple-structured compressive sensing-based channel estimation for RIS-aided MU-MIMO systems," *IEEE Trans. Wireless Commun.*, vol. 21, no. 12, pp. 11 095–11 109, Dec. 2022.
- [18] H. Xie, F. Gao, and S. Jin, "An overview of low-rank channel estimation for massive MIMO systems," *IEEE Access*, vol. 4, pp. 7313–7321, 2016.
- [19] S. Zhao, N. Guo, X.-P. Zhang, X. Cui, and M. Lu, "Sequential Doppler-shift-based optimal localization and synchronization with TOA," *IEEE Internet Things J.*, vol. 9, pp. 16 234–16 246, Sep. 2022.
- [20] Y. Lin, S. Jin, M. Matthaiou, and X. You, "Tensor-based algebraic channel estimation for hybrid IRS-assisted MIMO-OFDM," *IEEE Trans. Wireless Commun.*, vol. 20, no. 6, pp. 3770–3784, Jun. 2021.
- [21] X. Xu, S. Zhang, F. Gao, and J. Wang, "Sparse bayesian learning based channel extrapolation for RIS assisted MIMO-OFDM," *IEEE Trans. Commun.*, vol. 70, no. 8, pp. 5498–5513, Aug. 2022.
- [22] L. Mo, F. Saggese, X. Lu, Z. Wang, and P. Popovski, "Direct tensor-based estimation of broadband mmWave channels with RIS," *IEEE Commun. Lett.*, vol. 27, no. 7, pp. 1849–1853, Jul. 2023.
- [23] Y. Lin, S. Jin, M. Matthaiou, and X. You, "Channel estimation and user localization for IRS-assisted MIMO-OFDM systems," *IEEE Trans. Wireless Commun.*, vol. 21, pp. 2320–2335, Apr. 2022.
- [24] X. Zheng, P. Wang, J. Fang, and H. Li, "Compressed channel estimation for IRS-assisted millimeter wave OFDM systems: A low-rank tensor decomposition-based approach," *IEEE Wireless Commun. Lett.*, vol. 11, no. 6, pp. 1258–1262, Jun. 2022.
- [25] F. He, A. Harms, and L. Y. Yang, "Slow-moving channel estimation via Vandermonde structured tensor decomposition in RIS-aided MIMO systems," *IEEE Access*, vol. 12, pp. 67 772–67 783, 2024.
- [26] M. Sorensen and L. De Lathauwer, "Blind signal separation via tensor decomposition with Vandermonde factor: Canonical polyadic decomposition," *IEEE Trans. Signal Process.*, vol. 61, no. 22, pp. 5507–5519, Nov. 2013.
- [27] X. Wei, D. Shen, and L. Dai, "Channel estimation for RIS assisted wireless communications—part I: Fundamentals, solutions, and future opportunities," *IEEE Commun. Lett.*, vol. 25, no. 5, pp. 1398–1402, May 2021.
- [28] Z.-Q. He and X. Yuan, "Cascaded channel estimation for large intelligent metasurface assisted massive MIMO," *IEEE Wireless Commun. Lett.*, vol. 9, no. 2, pp. 210–214, Feb. 2020.
- [29] P. Zheng et al., "JrCUP: Joint RIS calibration and user positioning for 6G wireless systems," *IEEE Trans. Wireless Commun.*, vol. 23, no. 6, pp. 6683–6698, Jun. 2024.
- [30] G. Mylonopoulos, C. D'Andrea, and S. Buzzi, "Active reconfigurable intelligent surfaces for user localization in mmWave MIMO systems," in *Proc. IEEE Workshop Signal Process. Adv. Wireless Commun. (SPAWC)*, Jul. 2022, pp. 1–5.
- [31] Z. Zhang et al., "Active RIS vs. passive RIS: Which will prevail in 6G?" *IEEE Trans. Commun.*, vol. 71, no. 3, pp. 1707–1725, 2023.
- [32] Z. Peng, X. Liu, C. Pan, L. Li, and J. Wang, "Multi-pair D2D communications aided by an active RIS over spatially correlated channels with phase noise," *IEEE Wireless Commun. Lett.*, vol. 11, no. 10, pp. 2090–2094, Oct. 2022.
- [33] Z. Huang, B. Zheng, and R. Zhang, "Transforming fading channel from fast to slow: IRS-assisted high-mobility communication," in *Prof. IEEE Int. Conf. Commun. (ICC)*, Jun. 2021, pp. 1–6.
- [34] Z. Wan, Z. Gao, and M.-S. Alouini, "Broadband channel estimation for intelligent reflecting surface aided mmWave massive MIMO systems," in *Prof. IEEE Int. Conf. Commun. (ICC)*, Jun. 2020, pp. 1–6.
- [35] Y. Lu, H. Chen, J. Talvitie, H. Wymeersch, and M. Valkama, "Joint RIS calibration and multi-user positioning," in *Proc. IEEE Veh. Technol. Conf (VTC-Fall)*, Sep. 2022, pp. 1–6.
- [36] T. G. Kolda and B. W. Bader, "Tensor decompositions and applications," *SIAM Rev.*, vol. 51, no. 3, pp. 455–500, Aug. 2009.
- [37] F. Wen, N. Garcia, J. Kulmer, K. Witrissal, and H. Wymeersch, "Tensor decomposition based beamspace ESPRIT for millimeter wave MIMO channel estimation," in *Prof. IEEE Global Commun. Conf. (GLOBECOM)*, Dec. 2018, pp. 1–7.
- [38] F. Wen, H. C. So, and H. Wymeersch, "Tensor decomposition-based beamspace ESPRIT algorithm for multidimensional harmonic retrieval," in *Proc. IEEE Int. Conf. Acoust. Speech Signal Process. (ICASSP)*, May 2020, pp. 4572–4576.
- [39] T. Jiang, N. Sidiropoulos, and J. ten Berge, "Almost-sure identifiability of multidimensional harmonic retrieval," *IEEE Trans. Signal Process.*, vol. 49, no. 9, pp. 1849–1859, Sep. 2001.
- [40] M. Wax and T. Kailath, "Detection of signals by information theoretic criteria," *IEEE Trans. Acoust. Speech Signal Process.*, vol. 33, no. 2, pp. 387–392, Apr. 1985.
- [41] Z. Zhou, J. Fang, L. Yang, H. Li, Z. Chen, and R. S. Blum, "Low-rank tensor decomposition-aided channel estimation for millimeter wave MIMO-OFDM systems," *IEEE J. Sel. Areas Commun.*, vol. 35, no. 7, pp. 1524–1538, Jul. 2017.
- [42] S. M. Kay, *Fundamentals of statistical signal processing: Estimation theory*. Hoboken, NJ, USA: Prentice Hall, 1993.
- [43] Z. Huang, B. Zheng, and R. Zhang, "Transforming fading channel from fast to slow: Intelligent refracting surface aided high-mobility communication," *IEEE Trans. Wireless Commun.*, vol. 21, no. 7, pp. 4989–5003, Jul. 2022.
- [44] R. A. Horn and C. R. Johnson, *Matrix analysis*. Cambridge, U.K.: Cambridge Univ. Press, 2012.
- [45] N. Vervliet, O. Debals, L. Sorber, M. Van Barel, and L. De Lathauwer, "Tensorlab 3.0," Mar. 2016. [Online]. Available: <https://www.tensorlab.net>
- [46] N. Boumal, B. Mishra, P.-A. Absil, and R. Sepulchre, "Manopt, a Matlab toolbox for optimization on manifolds," *J. Mach. Learn. Res.*, vol. 15, no. 42, pp. 1455–1459, Apr. 2014. [Online]. Available: <https://www.manopt.org>